N⁰ d'ordre NNT : xxx

THÈSE DE DOCTORAT DE L'UNIVERSITÉ DE LYON
opérée au sein de
l'Université Claude Bernard Lyon 1

École Doctorale ED52
Physique et Astrophysique de Lyon

Spécialité de doctorat :
Discipline : Physique médicale

Soutenue publiquement à huis clos le jj/12/2018, par :
Mattia Fontana

Tests and characterization of gamma cameras for ion beam therapy monitoring and nuclear medicine applications

---

Devant le jury composé de :

Nom Prénom, grade/qualité, établissement/entreprise   Président(e)

Thirolf Peter, grade/qualité, établissement/entreprise   Rapporteur

Llosá Gabriela, grade/qualité, établissement/entreprise   Rapporteure

Morel Christian, grade/qualité, établissement/entreprise   Examinateur

Rafecas Magdalena, grade/qualité, établissement/entreprise   Examinatrice

Testa Étienne, grade/qualité, établissement/entreprise   Directeur de thèse

Létang Jean Michel, grade/qualité, établissement/entreprise   Co-directeur de thèse

Dauvergne Denis, grade/qualité, établissement/entreprise   Invité

Tests and characterization of gamma cameras for ion beam therapy monitoring and nuclear medicine applications

PhD Candidate

MATTIA FONTANA

Thesis directors

ÉTIENNE TESTA and JEAN MICHEL LÉTANG

Université Claude Bernard
Lyon 1
Physics departement
Doctoral school ED52:
Physics and Astrophysics

Abstract

Ion beam therapy is a promising technique in cancer treatment because of the ion defined range and favorable dose delivery features. Strict and precise treatment planning and monitoring are now key points for the method developments and full exploitation. In particular, with the aim of optimizing the ion treatment effectiveness, the ion range monitoring is mandatory: different solutions have been explored, but an online treatment check is still a challenge. The ion beam treatment monitoring is mainly performed by means of secondary charged or neutral particles. In this context, the detection of the prompt-gammas (PG) emitted during treatments has proven its potential in the ion range control in real time. Since the first evidence of the existing correlation between the emitted gamma profile fall-off and the Bragg peak position, several groups are involved in research activities in order to develop and optimize instruments and methods with the aim of improving this monitoring technique. Among the others, collimated and Compton cameras are being studied and optimized for this application. The same detectors can also be employed in nuclear medicine for the detection of the radioactive elements decay products.

A collaboration of 5 institutions in France is involved in the parallel development of two composite detectors for ion beam monitoring and nuclear medicine application, and this thesis is carried out within this collaboration with the detectors clinical trial as final aim.

The project started a few years ago and is now at the final stage. The two cameras have been designed according to simulation studies, and the different components are now under tests. The collimated camera is composed by a multi-slit tungsten mechanical collimator, set in front of an absorber composed of 96 BGO blocks, for a total size of 380x380x30 mm^3; each block presents a streaked surface with a 8x8 pixel matrix and the signal is read-out by 4 photomultipliers. A $\sim$3 ns time resolution can be achieved for the prompt gamma detection. The same absorber is part of the Compton camera, in addition to a scatterer section composed by 7 Double-Sided Silicon Detectors 96x96x2 mm^3 each. With the collimated camera, the parallel emitted photons are selected by the collimator and a mono-dimensional emission profile can be reconstructed. The Compton camera has a more efficient detection technique, being absent a mechanical collimation system, and could potentially lead to 3D information thanks to the reconstruction of the Compton cone. In both cases an additional detector component is needed to temporally tag the incoming beam ions and help rejecting the relevant background (mostly due to neutrons) which strongly affects the prompt gamma yield. A scintillating fiber tagging hodoscope is then under development: it is composed by 128x2 perpendicular scintillating fibers, read-out from both sides by 8 64-channel silicon photomultipliers by Hamamatsu. The thesis work consists in the critical evaluation, characterization and tuning of the different components, together with the associated electronics, and of the complete detectors on beam. In parallel, simulation studies can improve the detection technique and optimize the detector structure, as well as pave the way for further applications.

Contents

List of Figures

List of Tables

Prologue

1

Introduction

1.1 Ion beam therapy

1.1.1 Physics

1.1.2 Advantages and drawbacks

1.1.3 Range verification

1.1.4 Secondary radiations

1.1.5 Prompt-gammas: physics and features

1.1.6 State of the art of range verification

1.2 Nuclear medicine

1.2.1 PET and SPECT

1.2.2 Comparison, advantages and drawbacks

1.2.3 State of the art of SPECT

1.3 Photons

1.3.1 Photon interactions in matter

1.3.2 Photon detection

2

Gamma cameras

Contents

Figure 2.1: A cow licking its nose. Usage with permission of the photographer NICOLE BARTH, taken from www.flickr.com/photos/46311827@N07/14885545396.

In Figure 2.1 you see a cow that is licking its nose. The picture was taken by Nicole Barth on 11.08.2014 using a Canon EOS 500D. The original file has a resolution of 4247 × 2831 pixels.
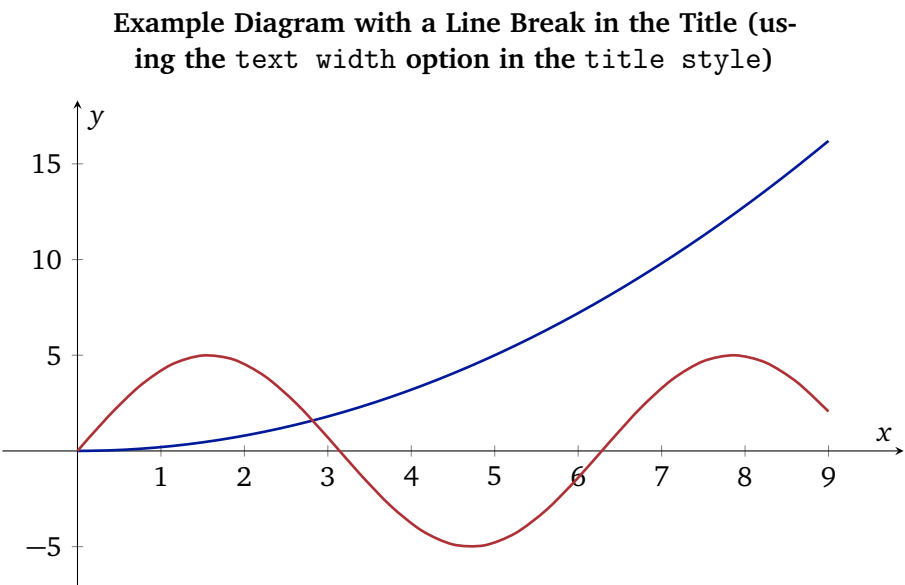
Figure 2.2: A scientific diagram using the `pgfplots` package by CHRISTIAN FEUERSAENGER using the same colors which are also used for the layout.

Item		
Animal	Description	Price ($)
Gnat	per gram	13.65
	each	0.01
Gnu	stuffed	92.50
Emu	stuffed	33.33
Armadillo	frozen	8.99

Table 2.1: A small table created with the `booktabs` package (example taken from the package documentation).

- First item in a list

- Second item in a list

- Third item in a list

- Fourth item in a list

- Fifth item in a list

1. First item in a list

2. Second item in a list

3. Third item in a list

4. Fourth item in a list

5. Fifth item in a list

Hello, here is some text without a meaning. This text should show what a printed text will look like at this place. If you read this text, you will get no information. Really? Is there no information? Is there a difference between this text and some nonsense like "Huardest gefburn"? Kjift – not at all! A blind text gives you information about the selected font, how the letters are written and an impression of the look. This text should contain and it should be written in of the original language. There is no need for special content, but the length of words should match the language. like this all letters of the alphabet

$$\bar{x} = \frac{1}{n} \sum_{i=1}^{i=n} x_i = \frac{x_1 + x_2 + \ldots + x_n}{n}$$

Hello, here is some text without a meaning. This text should show what a printed text will look like at this place. If you read this text, you will get no information. Really? Is there no information? Is there a difference between this text and some nonsense like "Huardest gefburn"? Kjift – not at all! A blind text gives you information about the selected font, how the letters are written and an impression of the look. This text should contain and it should like this all letters of the alphabet

be written in of the original language. There is no need for special content, but the length of words should match the language.

$$\int_0^\infty e^{-\alpha x^2}\mathrm{d}x = \frac{1}{2}\sqrt{\int_{-\infty}^\infty e^{-\alpha x^2}\mathrm{d}x \int_{-\infty}^\infty e^{-\alpha y^2}\mathrm{d}y} = \frac{1}{2}\sqrt{\frac{\pi}{\alpha}}$$

Hello, here is some text without a meaning. This text should show what a printed text will look like at this place. If you read this text, you will get no information. Really? Is there no information? Is there a difference between this text and some nonsense like "Huardest gefburn"? Kjift – not at all! A blind text gives you information about the selected font, how the letters are written and an impression of the look. This text should contain and it should be written in of the original language. There is no need for special content, but the length of words should match the language.

like this all letters of the alphabet

$$\sum_{k=0}^\infty a_0 q^k = \lim_{n\to\infty}\sum_{k=0}^n a_0 q^k = \lim_{n\to\infty} a_0 \frac{1-q^{n+1}}{1-q} = \frac{a_0}{1-q}$$

Hello, here is some text without a meaning. This text should show what a printed text will look like at this place. If you read this text, you will get no information. Really? Is there no information? Is there a difference between this text and some nonsense like "Huardest gefburn"? Kjift – not at all! A blind text gives you information about the selected font, how the letters are written and an impression of the look. This text should contain and it should be written in of the original language. There is no need for special content, but the length of words should match the language.

like this all letters of the alphabet

$$x_{1,2} = \frac{-b \pm \sqrt{b^2-4ac}}{2a} = \frac{-p \pm \sqrt{p^2-4q}}{2}$$

Hello, here is some text without a meaning. This text should show what a printed text will look like at this place. If you read this text, you will get no information. Really? Is there no information? Is there a difference between this text and some nonsense like "Huardest gefburn"? Kjift – not at all! A blind text gives you information about the selected font, how the letters are written and an impression of the look. This text should contain and it should be written in of the original language. There is no need for special content, but the length of words should match the language.

like this all letters of the alphabet

$$\frac{\partial^2 \Phi}{\partial x^2} + \frac{\partial^2 \Phi}{\partial y^2} + \frac{\partial^2 \Phi}{\partial z^2} = \frac{1}{c^2}\frac{\partial^2 \Phi}{\partial t^2}$$

Hello, here is some text without a meaning. This text should show what a printed text will look like at this place. If you read this text, you will get no information. Really? Is there no information? Is there a difference between this text and some nonsense like "Huardest gefburn"? Kjift – not at all! A blind text gives you information about the selected font, how the letters are written and an impression of the look. This text should contain and it should be written in of the original language. There is no need for special content, but the length of words should match the language.

like this all letters of the alphabet

2.1 Working principle

2.2 Applications in medicine

2.2.1 Ion beam therapy

2.2.2 Nuclear medicine

2.3 State of the art

3

CLaRyS prototypes

Contents

Following the highlighted limits of ion beam therapy (see chapter 1), a collaboration of five French research institutions was established in 2008 (**??**) with the aim of exploring different experimental solutions for the ion range online monitoring. The research group originally involved the "Institut de Physique Nucléaire de Lyon (IPNL)", the "Centre de Physique des Particules de Marseille (CPPM)", the "Laboratoire de Physique Subatomique et Corpuscolaire (LPSC)" in Grenoble, the "Laboratoire de Physique de Clermont (LPC)" and the "Centre de Recherche en Acquisition et Traitement de l'Image pour la Santé (CREATIS)" in Lyon. The collaboration focuses on the investigation of methods and detection solution for the online monitoring of ion beam range during ion beam therapy treatment, and is so called Contrôle en Ligne de lâhadronthérapie par Rayonnements Secondaires - Online monitoring of ion beam therapy through secondary particles (CLaRyS).

The main goal of the created collaboration is the parallel development of three gamma detection systems to be employed for ion range online monitoring purpose in the ion beam therapy field: a Positron Emission Tomography (PET) detector, a multi-collimated gamma camera and a Compton camera.

The design and development of the PET system is mainly managed by the LPC group, which left the collaboration in 2017, and the this detection system is not treated in this thesis work. In this chapter the two gamma cameras (multi-collimated and Compton) prototypes are described in details, and the present status of the instrumental development is presented. In the following, an entire chapter (chapter 6) is dedicated to the tests of the detectors performed on ion beams.

3.1 CLaRyS gamma cameras

The two gamma cameras under development by the CLaRyS collaboration are devoted to the detection of prompt-gamma rays emitted during ion beam treatments (see section **??**). The design of the two cameras has been optimized by different Monte Carlo simulation studies for what concerns both the detector components and the geometrical setup.

As already mentioned, a Compton camera is usually composed of two detector sections, a scatterer and an absorber: the CLaRyS prototype respects the standard design. In the scatterer, described in section 3.1.1, the prompt-gamma incoming ray is deflected by Compton interaction and the interaction position and energy deposited are stored. The scattered photon reaches then the absorber section, where its energy is ideally totally deposited and stored, again with the interaction position. This configuration is used to provide what is usually defined as "electronic collimation", but a mechanical collimation is still an option for photon detection and localization. The scatterer section can be replaced by a mechanical collimator, described in section 3.1.2, which selects the parallel incoming photons then absorbed by the same absorber detector (a geometrical setup adaptation is possible to optimize the detection performance and will be discussed in the following). The mechanically collimated system is called multi-collimated camera, due to the collimator multi-slit structure.

As underlined in section **??**, the prompt-gamma measurements are affected by several sources of background: in particular, the signals detected by the two cameras can come from secondary particles other then prompt-gammas, like photons from positron annihilation, neutrons and protons (for beam of ions heavier then protons). One of the possible solution for background rejection is the use of Time-Of-Flight (TOF) information (see section **??**), requiring a further detection section dedicated to the beam tagging. A beam tagging hodoscope is being developed in parallel and can be coupled to both the gamma cameras for TOF measurements; its

description is presented in section 3.1.4.
A schematic view of the two prototypes is given in figure 3.1.

3.1.1 Scatterer

The scatterer stack is one of the components of the Compton camera prototype. Dedicated to the photon Compton scattering, its design has been studied to optimize the Compton interaction probability in the energy range of interest and fulfill the camera requirements. The Compton events reconstruction strongly relies on the measurement of the energy deposited by the photon in its Compton interaction, mandatory to properly calculate the Compton scattering angle, which is then the aperture of the resulting Compton cone. The camera accuracy is then strictly dependent on the scattering energy resolution. At the same time, the camera efficiency is mainly due to the Compton interaction efficiency.

3.1.2 Collimator

3.1.3 Absorber

3.1.4 Beam tagging hodoscope

The Compton camera is composed of a scatterer part, which includes seven parallel planes of silicon detectors, $9\times9\times0.2$ cm^3, with 1 cm distance between the centers of two neighboring planes, and an absorber, composed of BGO blocks of size $3.5\times3.5\times3.0$ cm^3.

The following requirements governed the choice of silicon as scattering material, and BGO as absorber (Richard 2012):

- optimizing the single Compton event probability, without escape of the Compton electron from the detector where it is created;

- minimizing the Doppler effect (especially important for low energy gamma rays);

- obtaining the best possible energy resolution in the scatterer;

- ensuring the best possible spatial resolution in the absorber, also thanks to the maximization of the photo-effect absorption with the highest Z material.

Figure 3.1: Schematic view of the two CLaRyS gamma camera prototypes: the multi-collimated camera (top) and the Compton camera (bottom).
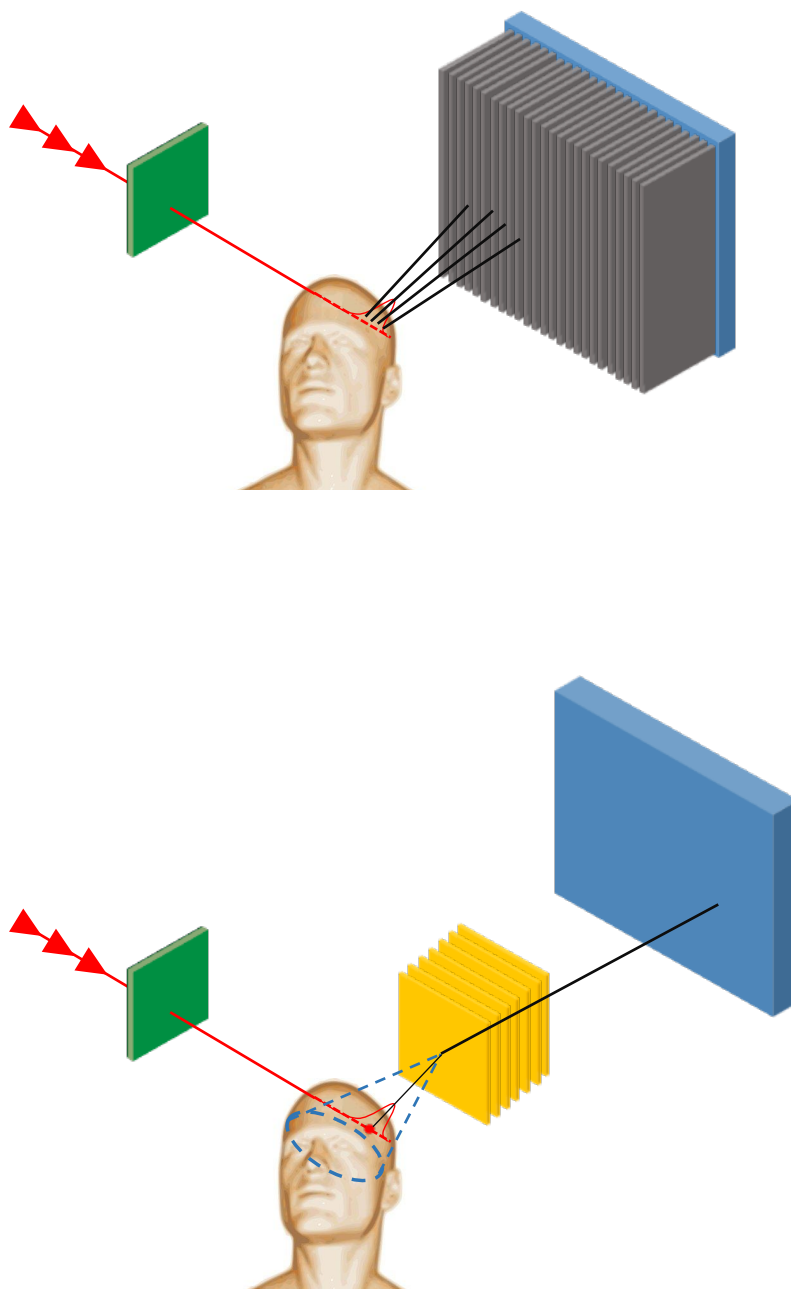
4

Compton camera application for ion beam therapy monitoring

5

Compton camera application in nuclear medicine

The results presented in this chapter have been published in (Fontana et al. 2017a) and (Fontana et al. 2017b).

Contents

Single Photon Emission Computed Tomography (SPECT) is one of the most widespread techniques for nuclear medicine diagnostics examinations. In most of the clinical cases, a radiotracer is injected in the patient and the emitted γ-rays are collected by scintillating detectors coupled to physical collimation systems. This process leads to the reconstruction of a planar transmission image. Such a kind of imaging tool relies on the first idea proposed by Hal Anger (Anger 1958, 1964), and it is now commercially available in different variants with peculiar features and applications. A complete system is often composed of at least two rotating detection heads, allowing a tomographic data acquisition and the reconstruction of a three-dimensional image of the radiotracer distribution (see chapter 1 for further details).

The main consequence of the collimation system is a forced trade-off between sensitivity and spatial resolution: The spatial resolution is completely determined by the collimator geometry, and it can only be increased by reducing the collimator hole size, at the expense of a reduction in the detector sensitivity since fewer photons survive the mechanical selection. Moreover, the collimator thickness and septa limit the primary energy acceptance, and the performance of Anger cameras generally downgrades as energy increases.

In order to overcome this mechanical collimator limitation, it is natural to move towards an "electronic collimation", where the emitted photons are tracked and the emission point is reconstructed via Compton kinematics, and so to the application of Compton cameras in this field (Everett et al. 1977; Singh 1983).

L. Han and colleagues (Han et al. 2008) have performed a simulation work comparing a standard Anger camera and a Compton camera prototype for a fixed source energy of 364 keV (iodine-131 gamma ray emission). The expected enhanced detection efficiency associated to the Compton camera with respect to the Anger system was estimated to a factor 20 at the tested energy, while the spatial resolution was compared for equal imaging time.

Starting from the results of Han and colleagues, we tested in simulation the performance of the CLaRyS Compton camera prototype (see chapter 3) for the application in SPECT. The aim of this simulation work consists in extending the aforementioned study to a wide energy range, with simplified analysis methods. The CLaRyS prototype is compared to the Infinia Anger camera delivered by General Electrics Healthcare (GE Healthcare 2006). The detector performances are compared in terms of efficiency and spatial response with the exposure to mono-energetic point-like radioactive sources at different energies, ranging from 245 keV to 2.614 MeV. The noise components related to the target (patient), such as photon attenuation, photon diffusion, patient movements, are common for both detectors and not considered in this context.

It should be noticed that the Compton detection principle requires coincidences between the two detector sections (scatterer and absorber), so that the random coincidence rate plays a fundamental role in the complete system performance, like in Positron Emission Tomography (PET) machines. The effect of these random coincidences will therefore be investigated. Moreover, a reliable Compton scattering cone reconstruction requires a precise energy resolution for the scatterer section of the detector. The influence of this parameter will be studied. Finally, the Doppler broadening effect will be quantified to give the physical limits of the Compton imaging technique knowing that silicon corresponds to the lowest Z material available for gamma detection with precise energy resolution. A comparison with a different possible scatterer material is also performed for verification.

All the obtained results are discussed with direct reference to (Han et al. 2008), focusing on the possible advantages offered by the use of a Compton camera (in particular the CLaRyS prototype), which intrinsically introduce the possibility to update the clinical standards in terms of source kinds, energies and activities, examination duration, patient dose, imaging techniques.

5.1 Material and methods

In this section, the sources of gamma rays simulated for the study are presented and discussed and the two simulated systems are described in detail, as well as the proposed analysis techniques. In addition to this, some comments are given about the criteria chosen to represent a relevant comparison between the two investigated detectors.

5.1.1 Radioactive sources

Both simulated systems have been exposed to monochromatic point-like gamma sources in air. The performance of the two cameras has been studied in terms of spatial resolution and detection efficiency as a function of the gamma source energy, related to actual radioemitters, already used in clinical practice or suggested for this kind of application in previous works (Nurdan et al. 2015). The explored energy range was chosen having in mind the possible clinical usage of Compton systems like the one developed by the CLaRyS collaboration, to extend the present field of application of SPECT imaging.

In table 5.1, the characteristics of the considered radioactive sources are given. Most of the sources do not emit gamma rays at a single energy, but only the ones selected for this study are presented in the table, together with the related branching ratio.

5.1.2 Compton camera simulation and data analysis

5.1.2.1 Simulation settings

The simulation code for the Compton camera was developed with GEometry And Tracking 4 (GEANT4) v.9.6 and the camera design is based on the specifications of the prototype at present under development by the CLaRyS collaboration, detailed in chapter 3. It should be noticed that the real size of the detector components slightly differs from the ones reproduced in simulation, which have been used in the code for simplicity. The geometric setting of the camera has initially been optimized for the application in ion therapy monitoring via prompt-gamma emission and has been adapted for SPECT for this study in order to maximize the similarities between the two systems (Compton and Anger camera) in terms of detector acceptance, as detailed in the following. A SPECT specific optimization would depend on the choice of the particular gamma energy and it has not been studied yet.

Table 5.1: Radioactive sources used in the comparison study. Decay mode list: EC for electron capture, $\beta-$ for electron emission, $\beta+$ for positron emission, IT for isomeric transition. Half-life expressed in days (d), hours (h) or minutes (m). Data extracted using the National Nuclear Data Center On-Line Data Service from the Evaluated Nuclear Structure Data File database, file revised as of (2017-05-17) (Bhat 1992).

Isotope	Gamma energy [keV]	Branching ratio [%]	Decay mode	Half-life
Indium 111	245	94.1	EC	2.8 d
Iodine 131	364	81.5	$\beta-$	8 d
Yttrium 91m	555	95.0	IT	50 m
Bismuth 212	727	6.7	$\beta-$	60 m
Iodine 132	773	75.6	$\beta-$	2.3 h
Iron 59	1099 - 1292	56.5 - 43.2	$\beta-$	45 d
Zinc 65	1116	50.0	EC / $\beta+$	244 d
Calcium 47	1297	67.0	$\beta-$	4.5 d
Magnesium 28	1342	54.0	$\beta-$	21 h
Sodium 24	1368	100.0	$\beta-$	25 h
Potassium 42	1524	18.1	$\beta-$	12 h
Thallium 208	2614	99.8	$\beta-$	3 m
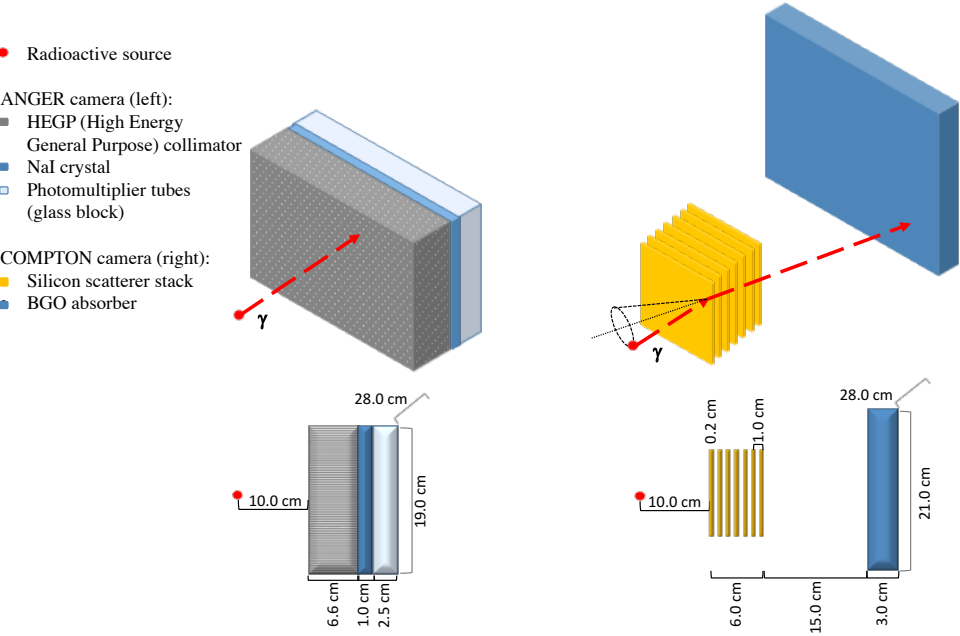
Figure 5.1: Sketch of the simulated geometry of the two systems: Anger camera (left) and Compton camera (right), in 3 dimensions (top line) and side projection (bottom line).

The distance between the last silicon plane (center) and the center of the absorber is set to 15 cm (see Figure **??**). Moreover, the absorber size has been adapted to be as close as possible to the Anger camera detector, maintaining the real Bismuth Germanium Oxide - $Bi_{12}GeO_{20}$ (BGO) block size. As a result, a matrix of 8×6 blocks has been arranged, for a total surface of 28×21 cm^2. In the work of Han and colleagues (Han et al. 2008) a Philips camera was described in GATE as Anger system and the same NaI absorber detector was adapted for the simulation of the Compton system with the introduction of silicon pad detectors as scatterer part. The two geometries compared in this study are slightly different but the common absorber size strategy has been maintained.

The values for energy and spatial resolution of the silicon and BGO detectors used in the simulation were derived from the first tests performed on the detector prototypes (see chapter 3). For the silicon planes, the energy resolution is obtained from the Equivalent Noise Charge (ENC):

$$\sigma_E = W_{Si}\sqrt{\text{ENC}^2 + F_{Si}\frac{E_{dep}}{W_{Si}}}, \tag{5.1}$$

where F_{Si} =0.115 is the silicon Fano factor, E_{dep} is the energy released in the detector (in eV) and W_{Si} is the energy required to create an electron-hole pair in silicon (3.6 eV). The ENC strongly affects the detector performance and it will be analyzed in the following.

The spatial resolution was set according to the geometric parameters considering that the employed double-sided silicon strip detectors have a total of 64 strips per side, with a pitch of 1.4 mm. The position of each interaction is set in the center of the strip where it is recorded in both detection planes. Charge sharing on neighbor strips can in principle allow for sub-pitch resolution, but according to preliminary characterization measurements the probability of such a kind of events is less than 10%. The interaction depth is set as the center of the involved detector slab. The time resolution has been set to 20.0 ns Full Width at Half Maximum (FWHM) based on characterization measurements performed at the Grand Accelerateur National d'Ions Lourds (GANIL) accelerator in France.

The energy and timing resolution in the BGO blocks are set to 21% FWHM and 3.0 ns FWHM respectively, also based on characterization measurements performed with a cesium-137 source (662 keV gamma ray emission) and at the GANIL with prototype blocks. The spatial resolution, as for the silicon planes, is not experimentally measured yet and it is therefore fixed to the size of a single pixel. Each block surface is streaked with an 8×8 pixel matrix, 4.4 mm side, not reproduced in the simulation code. Each interaction is assigned to the center of the pixel where it is localized at the analysis stage, while the interaction depth is set at the center of the involved block.

5.1.2.2 Data collection and analysis

The radioactive source is placed at 10 cm from the first silicon detector, in the center of the scatterer stack transverse surface, and the number of simulated primaries is set to 10^7 gammas per energy step. To speed up the simulation, the primary gammas are emitted in a direction

within the acceptance cone defined by the first Compton camera silicon plane. All results are then normalized to the full solid angle.

All the events with at least one interaction in a silicon plane or at least one interaction in a BGO block are stored during the simulation process in two data sets, one per detector section. A small fraction of events presents interactions in more than one scatterer plane ($< 1\%$ at 245 keV) and/or in more than one BGO block ($\sim$8% at 245 keV). This kind of events leads to ambiguities in the cone reconstruction, because the cone vertex and axis are not univocally defined, and it is not treatable via List Mode-Maximum Likelihood Expectation Maximization (LM-MLEM) reconstruction. Alternative reconstruction algorithms (such as the one included in the Medium-Energy Gamma-ray Astronomy library (MEGAlib) (Zoglauer et al. 2006)) are able to estimate the most likely scenario for multiple interactions, at the expense of larger uncertainties and longer calculation time. The multiple interactions events, representing approximatly 8% of the total at 245 keV, are then refused in this study for simplicity. This choice reduces the detection efficiency, so that the value obtained in this work could be seen as the lower limit for this kind of detection system. Once the two lists of events are built, the time coincidences are defined according to the source activity, the detector geometry and the single detection section time resolution. Finally, the emission points are reconstructed with a LM-MLEM algorithm developed by the Centre de Recherche en Acquisition et Traitement de l'Image pour la Santé (CREATIS) institute in Lyon (Lojacono et al. 2013). The iterative algorithm reconstructs the Compton cones from the position and energy deposited in the scatterer stack and in the absorber blocks. A reconstruction volume must be defined, as well as a voxel 3 dimensional matrix in this volume. For this study the reconstruction volume has been fixed to $5 \times 5 \times 5$ cm^3 around the source, with a matrix of $51 \times 51 \times 51$ voxels, and 15 algorithm iterations: this number is a compromise between reconstruction performance and calculation time.

5.1.2.3 Compton camera study for SPECT application

As already mentioned in the introduction, a critical parameter in the Compton camera performances is the scatterer detector energy resolution. The goal of the instrumental development is to obtain an energy resolution as close to 1 keV (σ_E) as possible. The silicon detectors composing the stack have been tested at various temperatures in order to understand the behavior of the electronic noise and of the leakage current, and the read-out electronics is being developed with the aim to reduce the electronic noise. The first laboratory tests showed an energy resolution at 25C of approximately 10-15 keV FWHM with a first read-out card prototype. The new card has been tested with simulated signals and gives a noise level closer to the expectations. No data are yet available to determine the detector energy resolution at different temperatures and with the final card version. In the simulation two different resolutions have been considered in order to verify the influence of this parameter on the final reconstructed image. The two chosen values are $\sigma_E = 2\,\mathrm{keV}$ and $\sigma_E = 4\,\mathrm{keV}$, corresponding to about 5 keV and 9.5 keV FWHM, respectively, both calculated at 200 keV of released energy using equation **??**. The influence of Doppler broadening has also been studied by disabling the Doppler effect in the simulation with the energy resolution set to $\sigma_E = 2\,\mathrm{keV}$. Finally, a different possible scatterer material, Cadmium Telluride (CdTe), has been tested at the same resolution in order to verify the expected advantage given by the choice of silicon.

A coincidence study is mandatory to define the source activity to be used in the simulations

dedicated to the benchmark with the Anger camera. Timing information is not included in the simulation code and a time structure must be assigned to the simulated primaries in the data analysis stage. A reference time is chosen randomly from an uniform distribution between 0 s and the data acquisition time and assigned to a primary photon. The data acquisition time (T_{DAQ}) is calculated as the expected time needed for the emission of the desired number of primaries ($N_{primaries}$) according to the source activity A_{source}:

$$T_{DAQ} = \frac{N_{primaries}}{A_{source}}.$$ (5.2)

The source activity is not fixed at the simulation stage but only during data analysis afterwards. It can therefore be easily modified to perform a study of the camera performance with different kinds of sources. The scatterer and absorber interaction times are calculated with respect to the reference primary emission and included in the related data sets for the analysis.

Two sets of data are produced as output of this analysis, one for the scatterer and one for the absorber: Each element in the two sets corresponds to an interaction in the detector and includes the interaction 3 dimensional position, energy released, time with respect to the total data acquisition time and primary reference index provided by the simulation. The elements in the two data lists are ordered for increasing time. The detectors time resolution specified in section **??** and a time window set to 20 ns, corresponding to a 3 σ acceptance are then used for the coincidence definition for different source activities. The time of each element in the absorber data set is compared to the time of the elements in the scatterer data set. A coincidence is defined when the scatterer event time is within the time window centered in the absorber event time. Each element is used one time only, and the analysis continues until the end of the absorber data list. If the two elements (one from the scatterer data set and one from the absorber one) forming a coincidence have the same reference index, they correspond to interactions of the same primary photons and the coincidence is then a true one. If the reference index is different for the two elements, the coincidence is random. The number of true and random coincidences has been studied as a function of the source activity in a range of clinical interest between 1 MBq and 500 MBq, for a fixed energy value of 555 keV. The variation of the influence of random coincidences as a function of the energy was also investigated at a fixed source activity of 200 MBq.

The scatterer energy resolution and the source activity have been fixed for the benchmark study. The choice of their values is discussed in section **??**.

5.1.3 Anger camera simulation and data analysis

5.1.3.1 Simulation settings

The Anger camera system is simulated with GEANT4 Application for Tomographic Emission (GATE) v.7.1 and it is based on the General Electrics Healthcare Infinia SPECT system (GE Healthcare 2006), a commercial clinical camera with parallel hole collimator and Sodium Iodide doped with Thallium (NaI(Tl)) scintillator. A single detection head is simulated in order to obtain a direct performance comparison to the Compton system.

The chosen configuration includes a High Energy General Purpose (HEGP) lead collimator, 6.6 cm thick, with a surface of 28×19 cm^2 (see Figure **??**). The parallel hole grid is composed of hexagonal shaped holes, 0.2 cm radius, arranged in a quincunx structure, with a septal thickness of 1.8 mm. This collimator is optimized for energies below 364 keV, corresponding to the main gamma emission energy of iodine-131. The NaI(Tl) crystal is simulated as a single block of 28×19×1 cm^3, in contact with the collimator back surface and read out by photo-multiplier tubes. The photo-multiplier grid is represented with a glass block of 2.5 cm thickness behind the crystal, with the same transverse surface (see Figure **??**). The spatial and energy resolutions have been set according to the manufacturer specifications. Unless otherwise stated, their values correspond to one standard deviation. A lower detected energy threshold has been set to 80 keV.

The source is placed at 10 cm distance from the collimator surface (the distance chosen in the Infinia data sheet), and its transverse position corresponds to the center of the central collimator hole. For each source energy, 10^8 primary photons are simulated in 4π. An event corresponds to single or multiple interaction of a photon (or secondary particle produced by the photon interaction in the collimator) in the NaI(Tl) crystal. All the detected interactions are computed and the gamma interaction position is calculated during the simulation as the center of gravity of the positions of all the hits (energy transfers of secondary electrons), with the deposited energy as weight for the calculation. The deposited energy corresponds to the sum of the energies released during each hit. A set of interaction points and energy deposited is then stored.

5.1.3.2 Data analysis

Four source primary energies have been chosen as references of the studied energy range and are used in the following to show the analysis method and the study results. The low energy range is represented by the indium-111 emission at 245 keV, the first energy above the Anger camera construction limit has been set to 555 keV (yttrium-91m), while iron-59 at 1099 keV and potassium-42 at 1524 keV have been chosen to represent the medium and high energy range respectively.

Figure **??** presents the raw radial event distributions for the four reference energies. Each distribution bin content is normalized according to the surface of the circular region corresponding to each radius. The first distribution bin always corresponds to the radius of the central collimator hole, with the partial inclusion of the surrounding septa. This choice is determined by the detector and collimator geometry and by the source position. It is possible to list three different kinds of events contributing to the radial distributions:

1. photons passing through the collimators holes without interactions,

2. photons traversing the collimator septa without interactions,

3. photons interacting in the collimator septa.

Only the first listed contribution transports true spatial information about the source location, and these photons generate the signal. All other kinds of events contribute to the background, which rapidly increases with the primary photon energy.

A background rejection is performed in order to extract the distribution corresponding to the signal. The complex background contribution cannot be determined analytically, we therefore approximated the background profile as a linear fit to the tail of the radial distribution. The fit limits have been defined as follows:

- the lower limit is calculated as the radial distance where the photon flux on the NaI(Tl) detector is reduced to a fraction $\frac{1}{e}$ by absorption effect in the collimator septa;

- the upper limit has been fixed to the half of the collimator smaller lateral side (95 mm), in order to avoid any kind of geometric effect due the binning choice or the normalization surface selection. The bin size creates artifacts in the radial distribution corresponding to the collimator limits, because three different geometries are involved: the circular surface covered by each distribution bin, the hexagonal shape of the collimator holes and the rectangular collimator geometry.

The estimated background profile is subtracted from the raw distribution and the result is used as reference of the image signal (figure **??**).

Two validation tests have been performed in order to check this analysis method. First, according to the geometry of the collimator and to the mass attenuation coefficient of NaI(Tl) (Hubbell et al. 1987), we evaluated the expected number of entries in the first distribution bin (before normalization), corresponding to the central collimator hole in front of the source. The calculation is performed with the attenuation law of photons in 1 cm of NaI(Tl). A dedicated set of simulations has been performed equivalent to the ones for the Anger camera described in section **??**, but using an ideal detector and a reduced number of photons of 10^7. No uncertainties are applied on the position of photon interactions to avoid resolution effects and the background is estimated via a linear fit as described above. The obtained entries in the first distribution bin after the fit selection are compared to the ones obtained with the theoretical calculation. In figure 5.3 the results are shown as a function of the source energy.

There is a good agreement between the values calculated with the attenuation law and the simulation data selected with the fit-based background subtraction, and the detected variations from the ideal trend are within the statistical fluctuations. A slight overall effect of under-detection is observed (about 10% on average), while the single value at 245 keV shows an opposite behavior (with a difference of less than 20%). This is related to the chosen fit function.

As a second validation, an additional set of simulations has been performed with the same settings as defined in section **??** but with an infinitely dense collimator. The raw radial distributions obtained with this set of simulation is compared to the radial distribution 'derived' by the simulations with nominal settings after the application of the fit-based background subtraction. The results are shown in figure 5.4.

It can be noticed that the distribution overall trend is reproduced by the fit-based background rejection method, the main source of difference being probably the contribution of the scattering in the hole grid surrounding the central one.

The linear fit appears to be a robust way to select the signal transporting spatial information

(a) 245 keV

(b) 555 keV

(c) 1099 keV

(d) 1524 keV
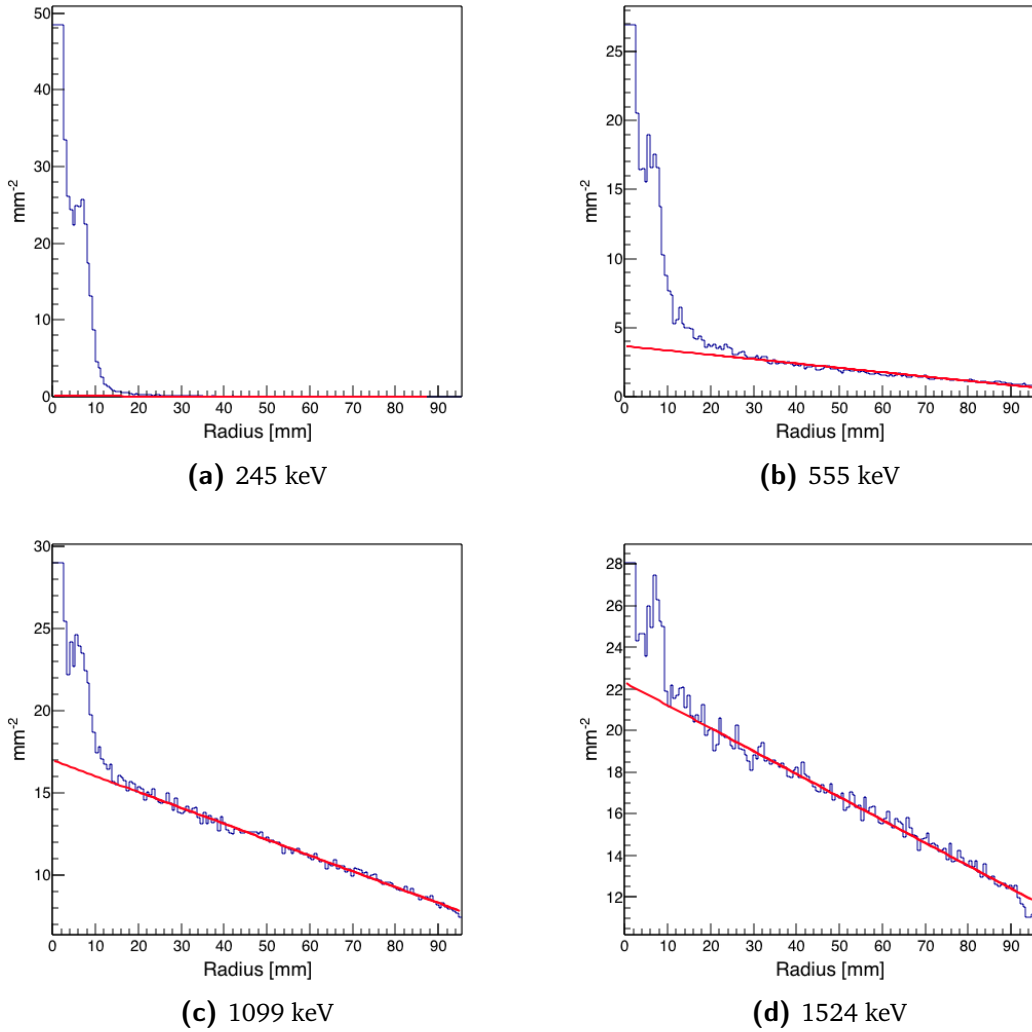
Figure 5.2: Radial event distribution normalized by the circular surface corresponding to each bin for 4 representative source energies, with the linear fit performed for background rejection. The total number of simulated primaries for each data set is 10^8.
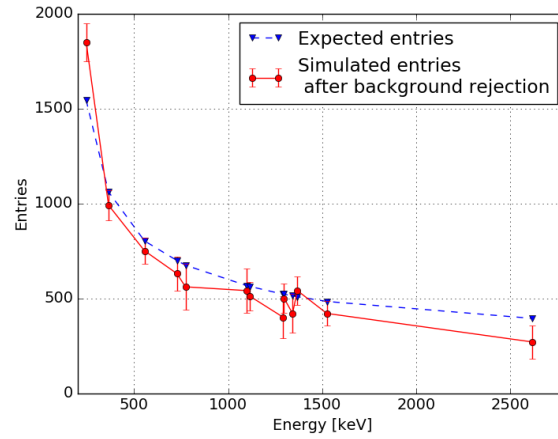
Figure 5.3: Comparison between expected entries in the central collimator hole (blue dashed curve) calculated according to pure geometrical factors and detector interaction cross section and simulated detected entries after background rejection (red solid curve) with null spatial resolution (ideal detector) to avoid resolution effects and lower energy threshold set to 80 keV.

from the source and is applied with no modification for the entire energy range, giving to the analysis method the desired consistency.

5.1.4 Figures of merit for the comparison study

The two cameras are studied and compared according to three figures of merit which refer to their main detection parameters: spatial resolution, detection efficiency, and signal-to-background ratio. The definition of these three values must be adapted to the two detectors, keeping in mind their differences: on one side the Anger camera provides a transmission image through a mechanical collimator, with no need for a reconstruction process and with a single detector component; on the other side, the Compton camera relies on event time-coincidences and needs a reconstruction algorithm to obtain the final spatial distribution.

In this study, the imaging process of a point source was simulated. The three figures of merit are therefore evaluated based on the radial event distribution, in order to profit of the radial symmetry of the simulated system.

For the Compton camera, the standard deviation of the radial distribution is used to express the detector spatial resolution, the detection efficiency is defined as the ratio between MLEM reconstructed events and total simulated primaries, and the signal-to-background ratio corresponds to the ratio between the number of reconstructed events and the total number of coincidences selected before the reconstruction with the coincidence analysis.

For the Anger camera, it is difficult to define the spatial resolution, as shown in (Cecchin et al. 2015). Here, we use the standard deviation of the signal radial distribution in order to be consistent with the Compton camera definition already proposed (the "signal" substantive means entries after background rejection). The detection efficiency is defined as the ratio between the number of signal events and the total number of simulated primaries. Finally, the signal-to-background ratio is evaluated as the ratio between the signal events (the entries

(a) 245 keV

(b) 555 keV

(c) 1099 keV

(d) 1524 keV
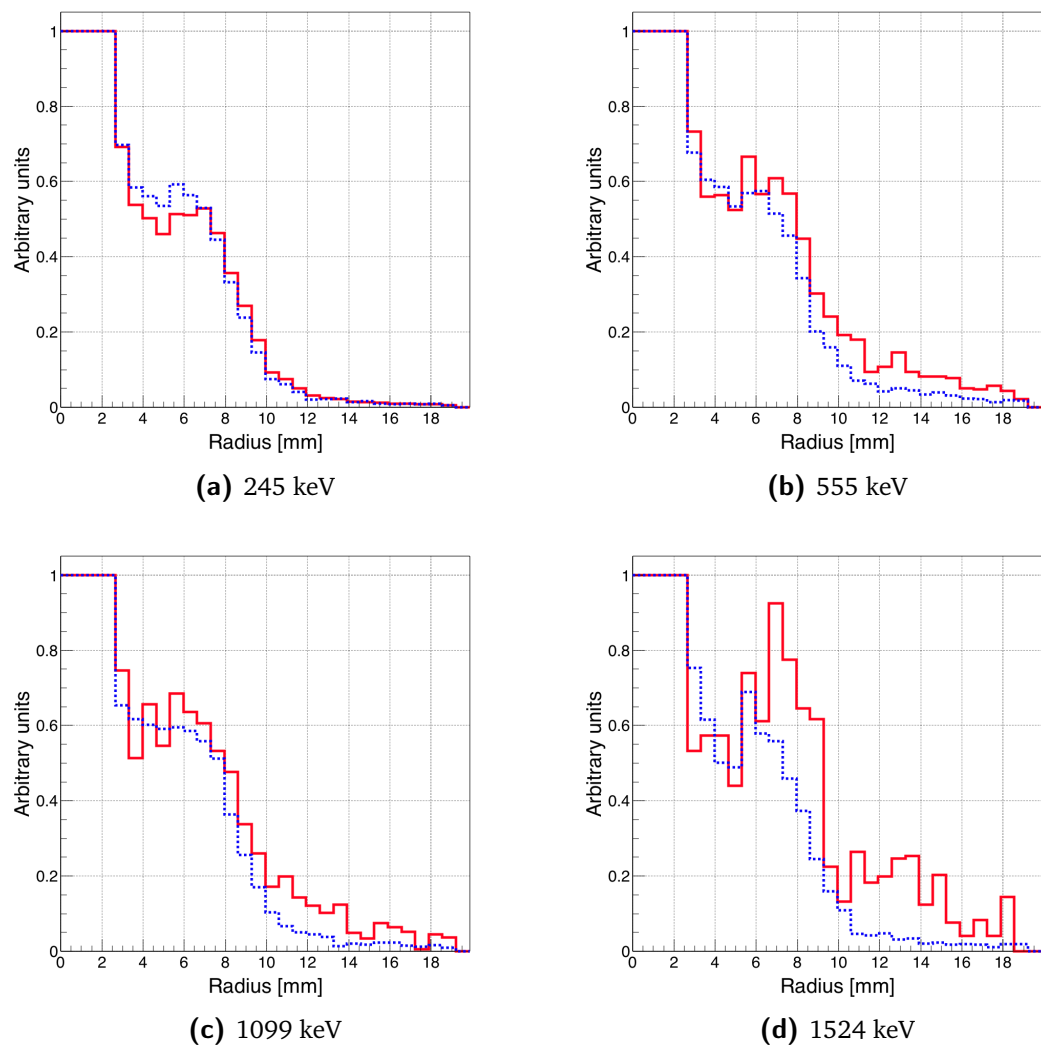
Figure 5.4: Normalized radial distribution with background rejection (red solid lines) compared to normalized radial distribution for infinite density collimator (blue dashed lines).

in the radial distribution after the fit-based background rejection) and the total number of events recorded by the detector (the entries in the raw radial distribution).

5.2 Results: Compton camera study for SPECT application

The results of the characterization of the CLaRyS Compton camera prototype for the application in SPECT are presented in the following sections, dedicated to the study of the scatterer detector energy resolution and of the Doppler broadening effect, and to the analysis of the rate of random coincidences, respectively.

5.2.1 Influence of Compton camera scatterer detector energy resolution

Figure **??** shows the standard deviation of the radial distribution obtained after the MLEM reconstruction (see section **??**) as a function of the source energy for the two different analyzed noise levels (Electron Noise Charge - ENC $= 500$ e$^-$, corresponding to $\sigma_E = 2$ keV, and ENC $=1100$ e$^-$, corresponding to $\sigma_E = 4$ keV). The maximum detected difference is about 35%, but the influence of the silicon detectors' energy resolution rapidly reduces at increasing energy. In the same figure, the results for the simulation without the Doppler broadening for the lowest energy resolution are shown. It is clear that this parameter has a strong influence for the Compton camera spatial resolution, at least for energies below 2.5 MeV. This result justifies the choice of silicon as scatterer material, because it is the lowest Z available detector and therefore minimizes the Doppler contribution. This is underlined by the black curve corresponding to a Cadmium Telluride (CdTe) detector, i.e. a higher Z material than silicon. For this last study, the electronic noise level has been set for CdTe in order to have the same intrinsic resolution as for silicon ($\sigma_E = 2$ keV obtained with equation **??**).
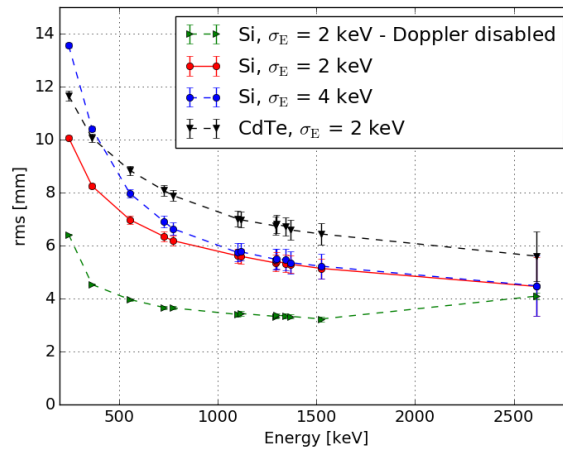
Figure 5.5: Reconstructed radial distribution standard deviation as a function of the source energy. Two energy resolution values are set to the silicon detectors ($\sigma_E = 2$ keV - red dots solid line - and $\sigma_E = 4$ keV - blue dots dashed line), the Doppler broadening effect has been removed (green horizontal triangles dashed line) and the scatterer material has been changed with CdTe solid state detectors (black vertical triangles dashed line), for a fixed energy resolution of $\sigma_E = 2$ keV.
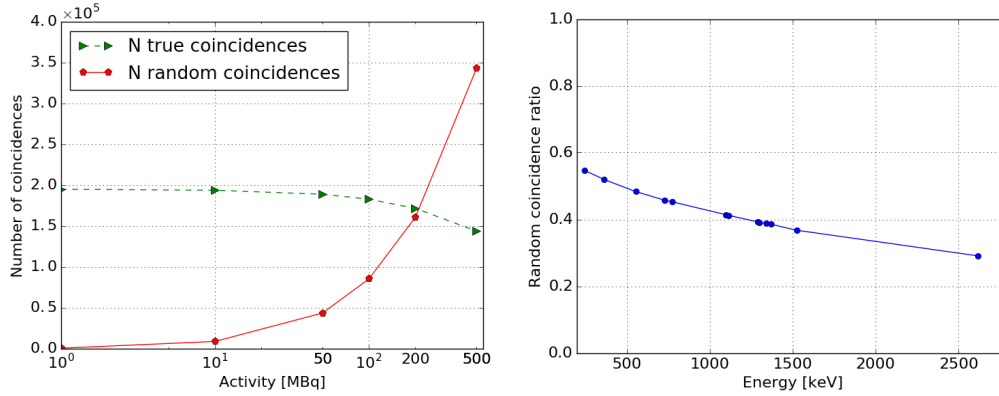
Figure 5.6: Left: number of true (green) and random (red) coincidences as a function of the source activity in the range 1-500 MBq, for the reference energy of 555 keV. Right: Percentage of random coincidences as a function of the source energy, with a fixed source activity of 200 MBq. Compton camera parameters: time resolution FWHM of 20 ns for silicon detectors, 3 ns for BGO and a coincidence window of 40 ns. The source branching ratio has been set to 100% for all sources for simplicity in the comparison of results.

For the benchmark with the Anger camera, the ENC value of the Compton camera scatterer components has been fixed to 500 e⁻, which corresponds to the expected level of noise affecting the silicon detectors at about 0C (the silicon detectors are cooled down with a thermal-controlled box) and with the final acquisition card (about 2 keV σ_E). This value has to be experimentally verified.

5.2.2 Compton camera coincidence study

Figure **??** (left) shows the numbers of true and random coincidences as a function of the source activity, ranging between 1 and 500 MBq in order to explore the whole range potentially employed in real examinations. The energy is set to 555 keV.

At 200 MBq source activity, the same amount of true and random coincidences is observed at 555 keV gamma energy. With activities above this value, the ratio between true and random coincidences is less than one. In principle the reconstruction LM-MLEM program can partially reject this kind of events and if we consider the expected important increase in detection efficiency guaranteed by the "electronic collimation", it results clearly that it is not worth to employ high activity sources (or that a smaller camera can be considered at the expense of the examination time).

For the further analysis and the final detector comparison, the source activity has been then set to 200 MBq, and the number of random coincidences is studied as a function of the source energy. Figure **??** (right) shows the ratio of detected random coincidences over the total number of reconstructed coincidences (see Section **??**) as a function of energy for a fixed activity of 200 MBq. The ratio decreases for increasing energies, because the product of independent interaction probabilities in two detectors decreases faster than the true coincidence one. Therefore, an increasing reconstruction efficiency with MLEM is verified (see Section **??**).

(a) Anger camera events.   **(b)** Compton camera reconstructed events.
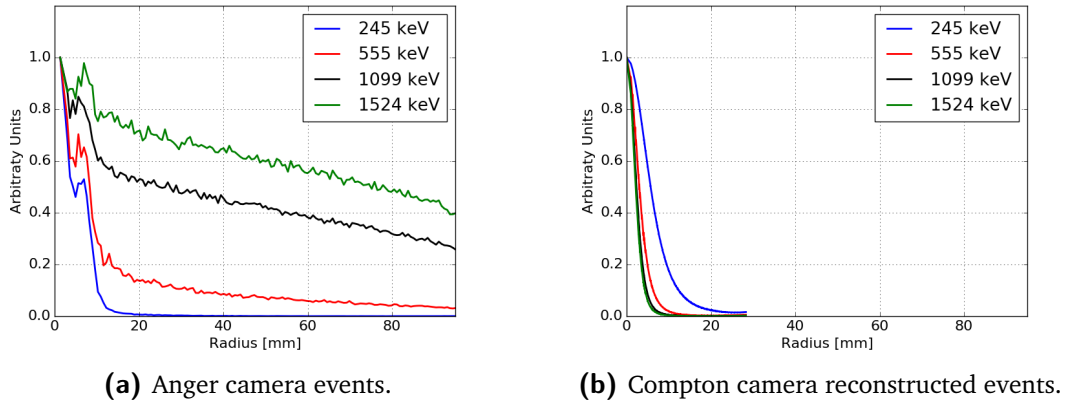
Figure 5.7: Overlap of the normalized radial distributions for 4 selected source energies.

5.3 Results: Benchmark of Compton camera and Anger camera performance

The analysis methods presented in section **??** and section **??** for the Compton and Anger camera, respectively, have been applied to the simulated data sets of the two cameras at all energies.

The radial distributions for Anger and Compton camera at the different reference source energies and a source activity of 200 MBq are shown in figure **??**. The same reference energies selected in section **??** are included here. The radial range is limited to the smaller collimator lateral size (95 mm), according to the fit limits imposed on the Anger camera data (see Section **??**). The curves are normalized to 1 for an easier visual comparison.

In figures **??**, **??**, and **??**, the detection efficiency, the radial distribution standard deviation and the signal-over-noise ratio are respectively shown as a function of the source energy for the two sets of data. Uncertainties (1 standard deviation) are reported for all the values and included in the data points when not visible.

From figure **??** one can point out the advantage provided by the absence of a physical collimation system in terms of detector efficiency. It should be noticed that two different scales are applied to figure **??** in order to show the two plots on the same figure and appreciate the variations with respect to the energy. The detection efficiency of the Compton camera is always more than a factor 20 higher than the one of the Anger camera. Although the images of the Anger and Compton cameras are based on different kinds of spatial information (a line and a cone, respectively), the Compton camera efficiency should allow a substantial reduction of the injected source activity and/or of the acquisition time. The efficiency of both cameras constantly decreases with increasing energy, because of the decreasing photon interaction probability. The only exception is found at the lowest considered energy of 245 keV in the Compton camera, due to an increased probability of photon absorption in the scatterer and, in parallel, a larger fraction of events with wide Compton scattering angles at low gamma energy.

The standard deviation of the radial distribution, shown in figure **??**, confirms the optimiza-

31
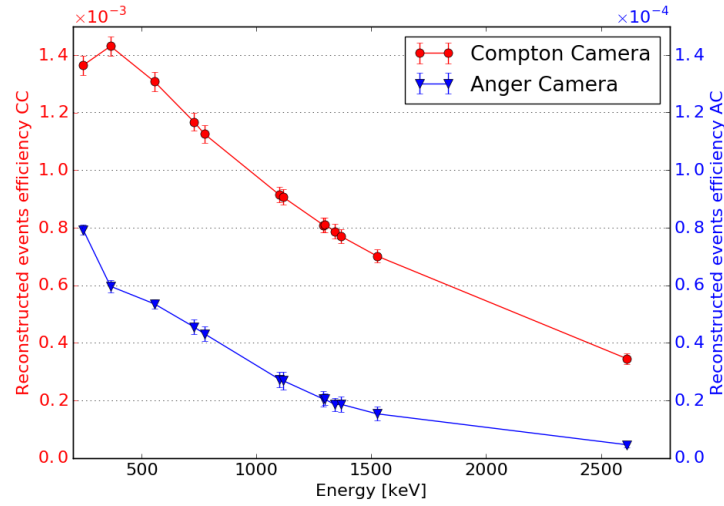
Figure 5.8: Detection efficiency as a function of the source energy. Source activity = 200 MBq, Compton camera silicon detector $\sigma_E = 2\,\text{keV}$.
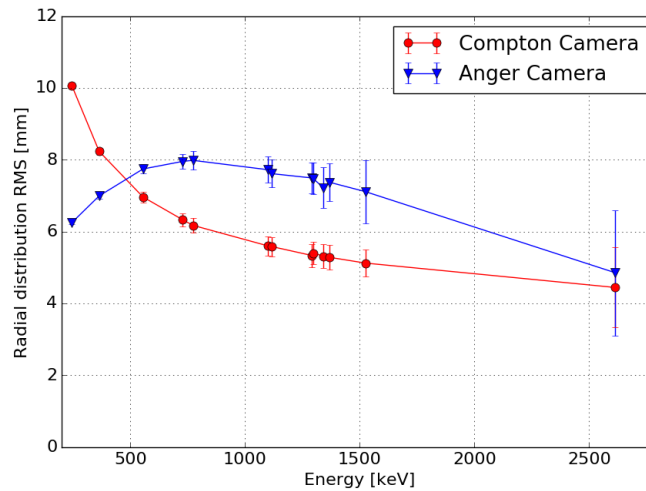
Figure 5.9: Standard deviation of the radial event distributions as a function of the source energy. Source activity = 200 MBq, Compton camera silicon detector $\sigma_E = 2\,\text{keV}$.

tion of the chosen collimator for the Anger camera for low energies (below 364 keV). With the ad-hoc background subtraction operated here, which is not realistic for an extended source, the Anger camera outperforms the Compton one in terms of spatial resolution at low energies (by > 3 mm at 245 keV and about 1.3 mm at 364 keV). However, above 500 keV, the Compton camera can provide a better spatial resolution with a difference ranging between a fraction of millimeter up to about 2 mm. For energies above 1.5 MeV, the two curves of standard deviation for the two cameras reach similar values (< 0.5 mm difference at 2614 keV), but figure **??** shows how the background rejection for the Anger camera and the MLEM reconstruction for the Compton system (see Sections **??** and **??**) affect this result. Above 364 keV, the selection for the background rejection of the Anger camera data drastically reduces the number of events contributing to the final image (the ratio between selected and detected events approaches zero). With an extreme selection, at very high energy the only events contributing to the final image are the events traversing the central hole of the collimator, resulting in an enhanced
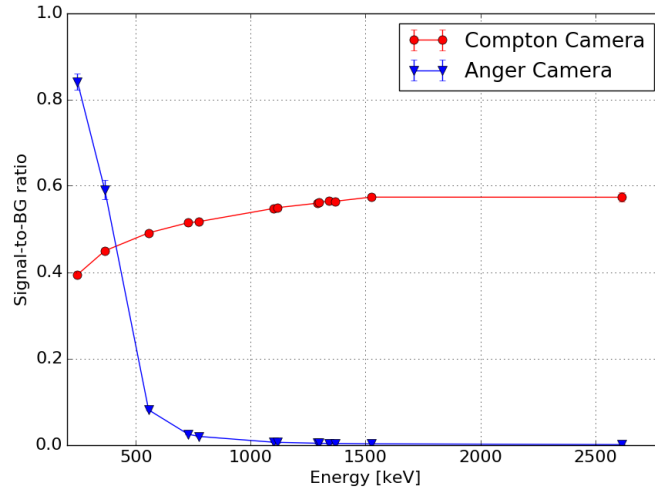
Figure 5.10: Signal-to-background ratio as a function of the source energy. Source activity = 200 MBq, Compton camera silicon detector $\sigma_E = 2\,\text{keV}$.

spatial resolution (see Figure **??**). The signal-to-background ratio of the Compton camera confirms the expectations concerning the reconstruction algorithm performance: if compared to Figure **??** (right), the curve in Figure **??** shows how the rejected events correspond approximately to the amount of random coincidences.

5.4 Discussion

The Compton camera under development by the CLaRyS collaboration is now at the characterization stage. Originally designed and optimized for the application in ion beam therapy monitoring for the detection of prompt-gamma rays in a wide energy range (between some hundreds of keV until about 10 MeV), it is here studied as SPECT detector in comparison to a commercial system based on the Anger gamma camera design.

The expected significant enhancement in terms of detection efficiency, for comparable imaging performance in terms of spatial accuracy, has been already proven in simulation in (Han et al. 2008) with a silicon-sodium iodide based Compton camera prototype at a single primary energy of 364 keV. A factor 20 efficiency gain has been reported.

First of all, the present work aimed to extend these results by testing the two detectors at increasing primary gamma energies, ranging from 245 keV to 2614 keV. A common analysis method has been defined in order to obtain comparable results, always keeping as reference the final image. The results were directly compared in terms of detection efficiency, spatial resolution (standard deviation of the radial event distribution) and event selection (background rejection for the Anger camera and Maximum Likelihood Expectation Maximization - MLEM - algorithm selection for the Compton camera) via the definition of three figures of merit.

A preliminary study has been performed on the simulated Compton camera data in order to fix the main parameters of the camera simulations, namely the energy resolution of the silicon

scatterer detectors and the source activity determining the coincidence rate. Two Electron Noise Charge values have been studied, resulting in a maximum difference in spatial resolution of 35% at the lowest energies, rapidly decreasing at increasing primary energy. A value of ENC = 500 e$^-$ has been chosen as the closest to the instrumental development expectations and first tests. The influence of the Doppler broadening on the spatial resolution has been also estimated in a factor $\sim$1/3 at 500 keV, then reduced up to $\sim$0 at 2.5 MeV of primary gamma energy, with fixed energy resolution ($\sigma_E = 2\,$keV - ENC = 500 e$^-$) in the silicon detectors. Moving to the coincidence rate analysis, at the reference energy of 555 keV and with detector time resolution set according to first characterization results, the simulated data have been analyzed by reproducing a source activity in the range 1-500 MBq. The result shows the expected increase in the random coincidence rate at increasing source activity, with a ratio between true and random coincidences close to one at 200 MBq. This value has been chosen as clinical reference for the comparison analysis.

The results discussed in section **??** confirm the conclusion of Han et al. about the advantage given by the usage of a Compton system and show how the gain factor in the detector efficiency is maintained at increasing energy. Concerning the detector spatial resolution, the Compton camera outperforms the Anger system at energies above about 500 keV. The Anger camera spatial resolution can be boosted by aggressive background subtraction in the considered case (point-like source image), at the expense of a drastic signal suppression. However, this approach is not reproducible and exploitable in actual clinical conditions and the obtained results are not comparable to the Compton camera performance at the same energy.

The results of this work clearly show the potential of the Compton camera for the application in nuclear medicine examination, opening new possibilities for the clinical implementation. The studied detector has originally been designed and optimized for another application, and it has only been adapted for SPECT here, but not yet optimized in terms of detector geometry (size, position, and inter-detector distances). For an optimized detector, performance is therefore expected to be improved with respect to the presented results. In future development, the reconstruction MLEM algorithm should be adapted to this application and the reconstruction parameters should be studied to further enhance the final performance, in particular for what concerns random coincidence rejection.

Anyway, these first evidences already allow one to investigate the possible modifications introduced by the clinical set of Compton detection systems. The enhanced detection efficiency in parallel with comparable spatial performances paves the way to the diffused usage of less active sources, or alternatively allows a substantial reduction of examination time: as a result, the dose delivered to the patient would be reduced. On the other side, the possible introduction of sources with higher primary emission energy will reduce the effect of photon attenuation in the patient (not studied in this simulation work), improving by definition the spatial information and further reducing the effective dose delivered to the patient. Simple analytic calculations can show how a photon attenuation of about 66% is foreseen for 364 keV photons in 10 cm of water, while the effect is reduced, for example, to 49 % at photon energy of 1099 keV (Hubbell et al. 1987). Higher energies can be employed also with Anger cameras, at the expense of introducing thicker collimators with reduced holes size, with the result of a reduced efficiency with respect to the analyzed High Energy General Purpose collimator. Furthermore, a possible implementation of Compton cameras is also foreseen for targeted radionuclide therapy, where the radionuclides used in clinics often have gamma radiation emission at relatively high energy. This signal is difficult to be detected and treated with

conventional SPECT cameras, while the Compton detection technique could make it quantitatively exploitable in clinical practice, for both pre- and per- treatment images.

Even though Compton cameras intrinsically lead to 3 dimensional images with a single detector head, the spatial resolution associated to the direction normal to the detector planes has to be more deeply studied, but this feature is an additional point in favor of the introduction of Compton systems in the clinical environment, moving beyond the tomographic concept and towards more compact detector solutions. Several studies are ongoing in order to improve the image reconstruction algorithms and, so, the 3 dimensional imaging performance (Kuchment et al. 2016). Different detection approaches can also, in principle, lead to improved image quality in 3 dimensions, such as the Compton electron tracking (Kabuki et al. 2007; Sonoda et al. 2015). Moreover, a further enhancement in image reconstruction should be given by the measurement of the photon depth of interaction: the photon is assumed to interact in the center of the detector components for our prototype, while perpendicularly segmented detectors can ensure an improved resolution in the third dimension and a resulting enhanced reconstruction accuracy, also involving better 3 dimensional imaging capabilities.

The advantages of the Compton detection principle are here shown thanks to a first detector prototype, but there is still wide room for improvement.

Once the CLaRyS Compton camera will be completed and characterized, tests in clinical environment are foreseen in the field of medical imaging. The actual potential of such a kind of detector will be then quantified with experimental data.

6

Beam tests

Contents

6.1 Hodoscope: december 2017

6.2 Hodoscope: may 2018

6.3 Collimated camera: august 2018

6.4 Collimated camera: september 2018

7

Conclusions and discussion

<div align="right">

A

</div>

Compton camera data format

A.1 Introduction

This document aims to formalize and fix the Compton camera data format. The structure of the data sent by each detector section (scatterer, absorber and beam hodoscope) to the acquisition card is detailed, as well as the structure of the events sent to the acquisition PC.

A.2 General features

A.2.1 Common information

The detector Front End cards are connected to the μ-TCA via optical links, with a speed of 3.0 Gbit/s. The transfer frequency is 150 MHz.
All the Front End card TDCs share the same synchronized clock, at a 40 MHz frequency, which is sent to the cards through an external link.
Every data packet sent to the μ-TCA by the Front End cards starts with the following information:

- N° Front End (8 bits);

- N° Trigger (24 bits);

- N° Mode (8 bits);

- N° of element in the packet (8 bits).

A.2.1.1 Front End number

The Front End number is the identification code of each Front End card. A mechanical switch on the card defines the ID which is sent in the data packet header.
In Table A.1 the Front End number IDs are listed with the corresponding cards.

Table A.1: Front End number associated to each Front End card.

FE number	FE card
0	All detectors
1	Silicon 1
2	Silicon 2
3	Silicon 3
4	Silicon 4
5	Silicon 5
6	Silicon 6
7	Silicon 7
8	Silicon 8
9	Silicon 9
10	Silicon 10
11	ASM 1
12	ASM 2
13	ASM 3
14	ASM 4
15	ASM 5
16	ASM 6
17	ASM 7
18	ASM 8
19	ASM 9
20	ASM 10
21	ASM 11
22	ASM 12
23	ASM 13
24	ASM 14
25	ASM 15
26	ASM 16
27	Hodoscope 1
28	Hodoscope 2
29	Hodoscope 3
30	Hodoscope 4
31	Hodoscope 5
32	Hodoscope 6
33	Hodoscope 7
34	Hodoscope 8
99	μ-TCA

A.2.1.2 Pre-trigger and trigger

The trigger number identifies each event, where an event is generated every time a coincidence is detected between a BGO block and a silicon layer. Once an interaction is detected in a BGO block, the associated ASM card generates a pre-trigger signal which is sent to the THOR card. This intermediate card shares the pre-trigger signal with the silicon FE cards; if an interaction with a compatible time stamp is found in one of the silicon layer, a trigger signal is generated and sent to all the silicon FE card, as well as to the ASM and hodoscope cards via the THOR card. The trigger signal validates the event, and each FE card sends the collected data to the μ-TCA system. The trigger number allows for a complete event reconstruction by the event builder on the acquisition PC. In Figure A.1 the trigger generation process is sketched.

To be noticed that each FE cards sends the collected data independently from the others.

Trigger and pre-trigger encoding

Pre-trigger and trigger signals are used by all the detectors to select the collected data to be sent to the acquisition system. The data selection and transfer must be as fast as possible in order to minimize the trigger latency and camera dead time. In order to reduce the transmission time, pre-trigger and trigger signals have been encoded on 24 bits.

This same trigger number is sent at the beginning of each data packet and is used by the event builder to associate the interactions collected by the three detector sections. With a 24-bit encoding, the trigger number is reset every 1 ns $\times 2^{24} = 16,78$ ms. This time window is short for the event builder, so that for the physical data it is extended to 32 bits for all the FE cards in order to have a reset every 1 ns $\times 2^{32} = 4,2$ s, which is enough for the reconstruction of the events.

A.2.1.3 Mode number

The Compton camera detector components can work in different mode, according to the application requirements. At least two working modes are possible for every detector section: an "optimal" mode, corresponding to the final camera configuration; a "test" mode, allowing for the collection of more raw information. Every operating mode presents a peculiar data format, so that the data packets size is not fixed. In order to fix the acquisition tuning, the mode number is defined before its beginning.

The operating mode are identified as following:

- N° Mode = 1 : 1st mode for silicon

- N° Mode = 2 : 2nd mode for silicon

- N° Mode = 3 : 3rd mode for silicon

- N° Mode = 4 : 4th mode for silicon

(a) An ASM card detects an interaction and sends a logical signal to the THOR card.

(b) The THOR card generates the pre-trigger signal.

(c) The pre-trigger is sent to the 10 silicon FE cards.

(d) A single silicon FE card generates the trigger.

(e) The trigger signal is distributed to all the detectors.

(f) The detectors send the collected data to the μ-TCA.
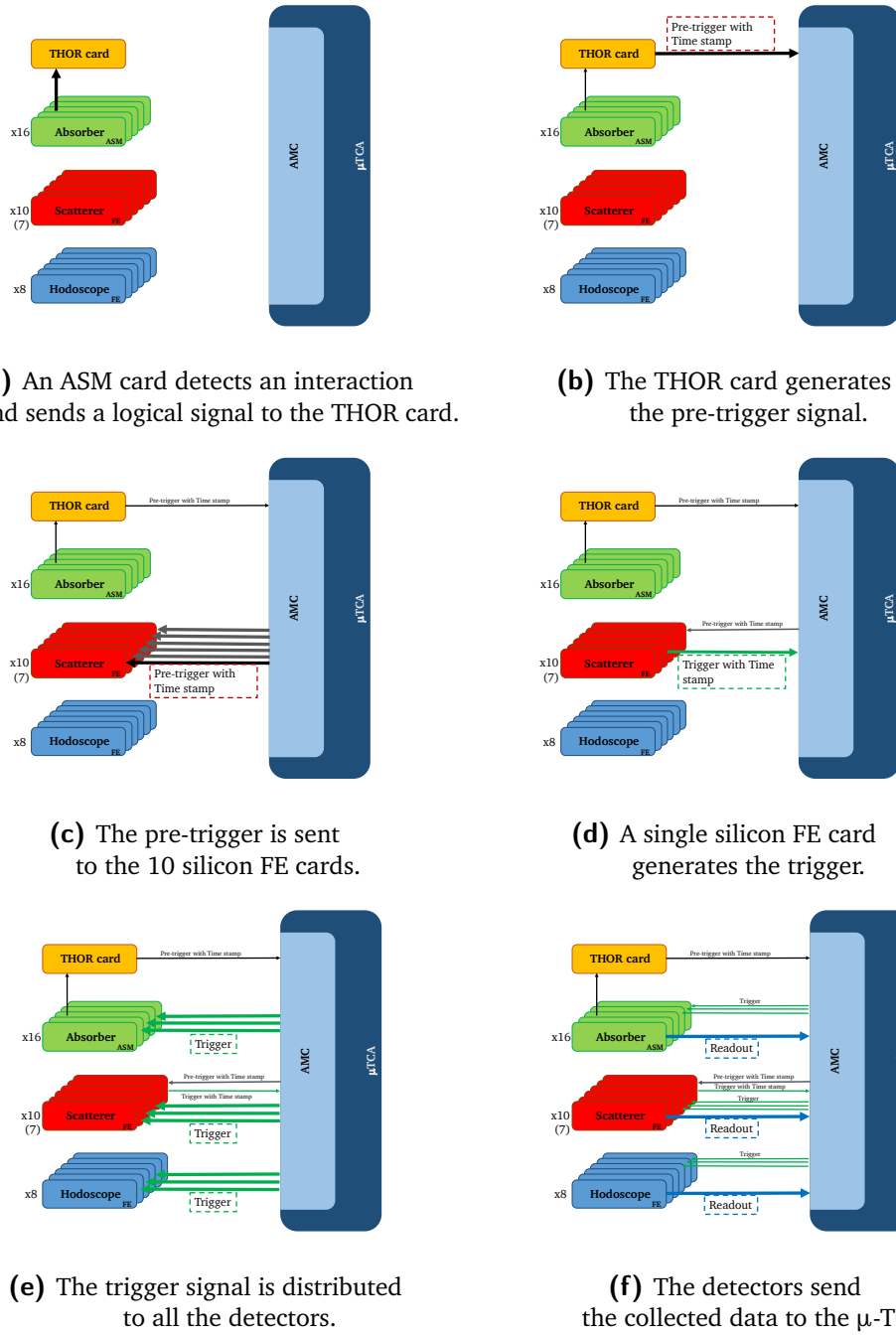
Figure A.1: Data acquisition logic: pre-trigger and trigger generation and readout process.

- N° Mode = 5 : 1st mode for BGO

- N° Mode = 6 : 2nd mode for BGO

- N° Mode = 7 : 1st mode for hodoscope

- N° Mode = 8 : 2nd mode for hodoscope.

A.3 Physical data format

A.3.1 Scatterer detector data format

Four different data formats, corresponding to four working modes, have been defined for the silicon scatterer operation (figure 2). For mode 1 and 2, the collected total charge is directly evaluated on the FE card via the slow shaper output and one ASIC, while for mode 3 and 4 the ASIC pre-amplifier output directly sends a sampling of the raw signal. In this last case, the number of samples can be tuned and each sample corresponds to 10 ns.The complete sampling is stored in a dedicated buffer (see table 9).

Modes 1 and 3
In mode 1 and 3, for each detector strip involved in the interaction, the strip ID, total collected charge and time are stored. The interaction position will be calculated via a center of gravity algorithm at the analysis stage. The raw information about the number of involved strips is useful for the evaluation of the signal dispersion in the detector.
Modes 2 and 4
In mode 2 and 4, the interaction is calculated on the FE card and the number of involved strip is then not stored.

A.3.2 Absorber detector data format

The BGO block readout is performed via the ASM cards. Each card is equipped with 24 input ports (signal PM), corresponding to 6 BGO blocks. Two possible working modes have been defined for the BGO absorber: the collected total charge and time are evaluated on the card, or the PM raw signals are sampled and the sampling is sent to the acquisition (figure 3). Charge and time are then calculated at the analysis stage. This second operating mode can be useful in the test phase but it determines a low acquisition rate, so that it can be used only at low beam intensity.
The complete sampling is stored in a dedicated buffer (see table 9).

A.3.3 Beam hodoscope data format

The beam tagging hodoscope is composed of two perpendicular planes of 128 scintillating fibers each. Each fiber is read-out on the two sides, for a total of 512 read-out channels. The output signals are send via optical fibers to 8 64-channel PM H8500 by Hamamatsu. 8 FE cards have been developed for the signal collection, one per PM, and are equipped with two custom ASICs (32 channels each) and one FPGA.
Concerning the "optimal" mode (1st operating mode for the hodoscope), the only collected information are the ID of the involved fibers and the interaction time. The ASICs allow for a minimum time resolution of 10 ns; this means that if two particles interacts in the hodoscope within a 10 ns window, they will be considered as part of a single event.

Mode 1

8 bits	24 bits	8 bits	8 bits	8 bits	16 bits	32 bits	

Mode 2

8 bits	24 bits	8 bits	8 bits	16 bits	16 bits	32 bits	

Mode 3

8 bits	24 bits	8 bits	8 bits	8 bits	16 bits	16 bits	32 bits	

Mode 4

8 bits	24 bits	8 bits	8 bits	16 bits	16 bits	16 bits	32 bits	
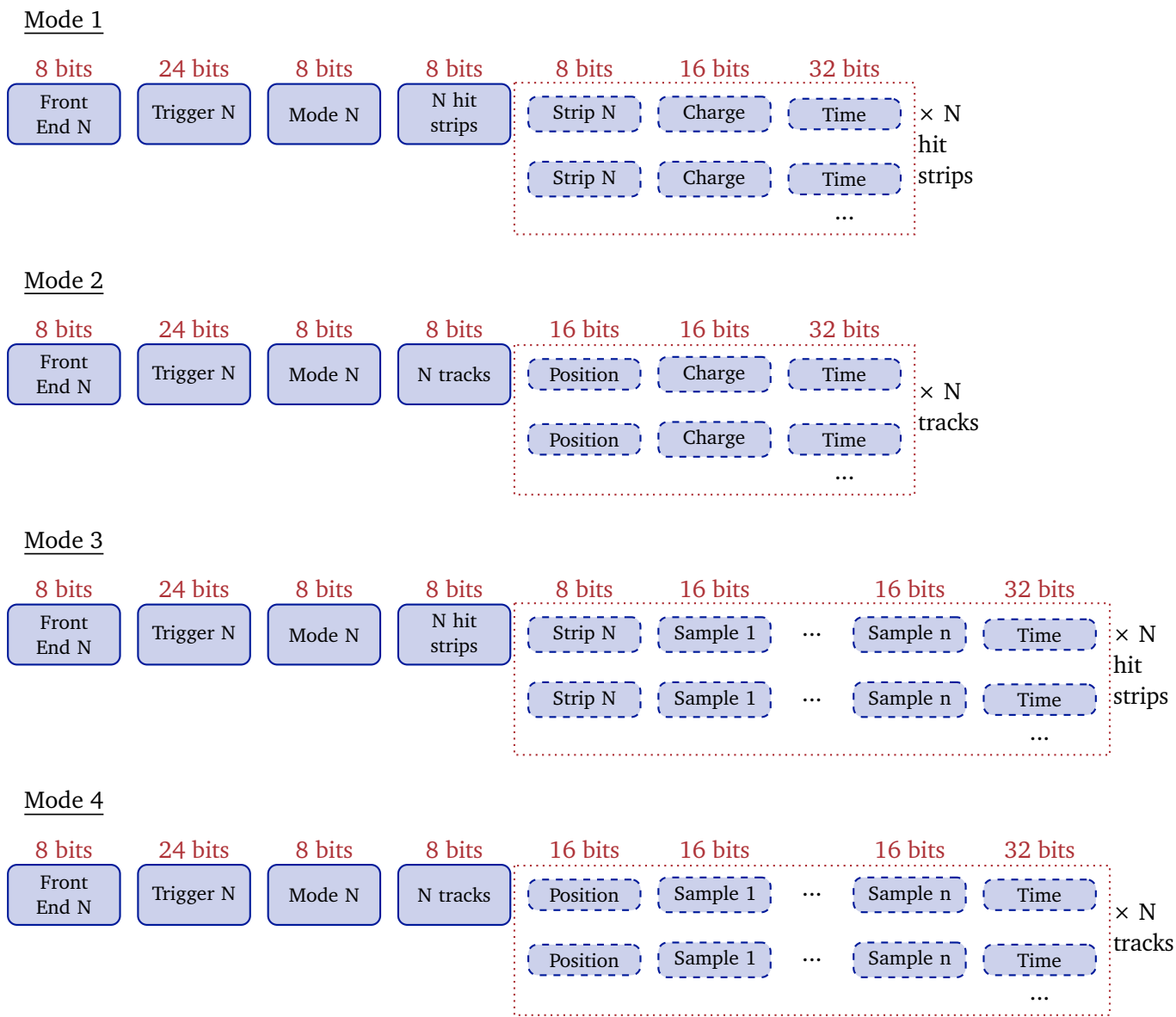
Figure A.2: Scatterer detector data format.

In test mode, the total collected charge can be calculated. This feature is useful to evaluate the detector aging effect due to radiation exposure. The charge measurement is anyway limited to a single channel per ASIC, so to two channels per PM. The ASIC channel able to measure the charge is identified as "N° Fiber charge 1" and "N° Fiber charge 2".

A.4 Slow control, trigger and monitoring data format

A.4.1 Communication architecture

The Endpoint architecture is composed of three layers:

- application layer

- mac (or transport) layer/processor packet

- physical layer

A.4.2 Transport protocol and processor packets

A.4.2.1 Definitions

It is worth to define some useful terms for the following part of the document:

- byte : 8 bits

- word : 16 bits

- K : control byte

- D : data byte

- cargo : data group

- terminator : packet end

- CRC : cyclic redundancy code

The CRC allows one to detect the transmission errors and the data transfer issues. A specific algorithm must be used, as CRC-16 : X16 + X15 + X2 + 1. In the present protocol, a "parity patter of 16 bits" have been used.

The transport layer ensures a proper packets exchange between two terminals via the data encapsulation. The data come from the application layer and are then sent to the physical layer.

A.4.2.2 Data encoding

For the transport layer, the data structure is created via the addition of a packet header, corresponding to a parity bit, of a 16 bit parity pattern and a bit for the end of the packet. The data are 8 bits/10 bits encoded. This standard 8 bits/10 bits encoding ensures sufficient data transitions for clock recovery.

A.4.2.3 Packets format

All the data packets have the same structure. A K byte (control symbol) is followed by the cargo to be sent. The end of the packets changes according to the cargo parity.
If the cargo contains an even number of bytes, the packet ends with K.28.6.

Table A.2: Packet with an even byte number cargo.

Item	Packet beginning	Cargo	Packet end
1	One K byte	0 - N D-bytes	K.28.6

If the cargo contains an odd number of bytes, the packet ends without any control symbol.

Table A.3: Packet with an odd byte number cargo.

Item	Packet beginning	Cargo	Packet end
1	One K byte	0 - N D-bytes	Beginning of a new packet

Remark :

- SYN packet is a special kind of packet starting with K.28.6 and ending with K.28.5. It is only composed of these two bytes (16 bits). It allows the receiver to find the beginning and the end of the transmitted bytes with the aim to reconstruct the events in parallel. The synchronization speed is 44 Hz (defined by Carlos Abellan).

- In order to optimize the throughput, the control symbol at the beginning of the packet can probably be removed (further study needed).

A.4.2.4 Possible control symbols

In the following table, all the possible control symbols are listed (defined by Carlos Abellan).

A.4.3 Transport layer

A.4.3.1 Control packet

This kind of packet is used to check the link and for the control/command operations.

- For the link check, two kinds of packets are used: synchronization packet and IDLE packet.

Table A.4: Control symbol definition.

Item	Name	Control code	Comment
1	K.28.0	0x1C	Acknowledgement
2	K.28.1	0x3C	Ask for writing registers
3	K.28.2	0x5C	Ask for reading registers
4	K.28.3	0x7C	Special command
5	K.28.4	0x9C	Monitoring
6	K.28.5	0xBC	Default synchronization
7	K.28.6	0xDC	IDLE (default) and packet end
8	K.28.7	0xFC	Pre-trigger
9	K.23.7	0xF7	Trigger
10	K.27.7	0xFB	
11	K.29.7	0xFD	
12	K.30.7	0xFE	Physical data

- For the control/command operations, here are some examples: register configuration, FPGA dynamical programming, monitoring, etc.

Control symbol for control :

Table A.5: Control symbol definition.

Item	Name	Control code	Comment
1	K.28.0	0x1C	Acknowledgement
2	K.28.1	0x3C	Ask for writing registers
3	K.28.2	0x5C	Ask for reading registers
4	K.28.3	0x7C	Special command
5	K.28.4	0x9C	Monitoring
6	K.28.5	0xBC	Synchronization
7	K.28.6	0xDC	IDLE (default) and end of packet

Acknowledgement packet (Front End cards → µ-TCA)

This packet is sent by the FE cards and interpreted as an acknowledgement by the µ-TCA. If a part is missing, it is set to zero.

- If 0 = validation

- If 1 = problem detected

Table A.6: Definition of the acknowledgement packet.

Word	1st byte	2nd byte							
		7b	6b	5b	4b	3b	2b	1b	0b
1	K.28.0	0	Pb Front End number	Pb with packet beginning	Pb with packet end	Pb with CRC	Pb with number of received words	Pb with parity bit of byte 2	parity bit of the acknowledgement packet
2		Front End number							

A.4.3.2 Configuration packets

Writing register process (μ-TCA → Front End cards)

The process starts with a packet sent by the μ-TCA asking for the register writing. The receiver (FE card) sends back an acknowledgement packet to finish the process. In the following table the format of this writing register packet is reported.

Table A.7: Writing register packet.

Word	1st byte	2nd byte	Comment
1	K.28.1	Front End number + 1 parity bit	N/A
2	2 bytes with the number of words to be written		The length is word-based: max $2^{16} - 1 = 65535$ words
3	Register address		Address where the writing process starts
4..N+3	Data to be written		0000 0000
N+4	CRC composed of the "xor" of all bits in the same position, from word 2 to word (N+3)		

Reading register process (μ-TCA → Front End cards)

The process starts with a packet sent by the μ-TCA asking for the register reading. The receiver (FE card) sends back the "measure packet" (Table 10) if the command is correct, an acknowledgement packet if it is not.
At the beginning of the slow control, the physical addresses on the FE cards are read at the address 0 (Table 9).
In the following table the format of this reading register packet is reported.

Table A.8: Reading register packet.

Word	1st byte	2nd byte	Comment
1	K.28.2	Front End number + 1 parity bit	N/A
2	2 bytes with the number of words to be read		The length is word-based: max $2^{16} - 1 = 65535$ words
3	Address of 1st data to be read		Address where the reading process starts
4	CRC composed of the "xor" of all bits in the same position, from word 2 to word 3		/

Table A.9: Two special registers(μ-TCA → Front End cards)

Register address	Details	Comment
0	Front End number	No writing rights: register in read-only mode. Hard coded on DAQ card.
1	It defines the working modes (Table 1)	Optimal mode, test mode, collimated camera mode, Compton camera mode, individual detector section test. It is possible to write in the register.
2	It defines the detector to test (in single detector test mode)	Scatterer, absorber, hodoscope.
3	BGO number of sampling	For test mode with the BGO blocks signal sampling.
4	Silicon number of sampling	For test mode with the silicon layers signal sampling.

Table A.10: Measurement packet (Front End cards → μ-TCA)

Word	1st byte	2nd byte	Comment
1	K.28.1	Front End number + 1 parity bit	
2	2 bytes for the number of data words to send		The length is word-based: max $2^{16} - 1 = 65535$ words
3	Register address		Address where the writing process starts
4..N+3	Read data		0000 0000
N+4	CRC composed of the "xor" of all bits in the same position, from word 2 to word (N+3)		/

A.4.3.3 Monitoring process (Front End cards → μ-TCA)

In case of issues, for example when the temperature of a card go beyond a fixed threshold, the DAQ card sends a "monitoring" packet to the μ-TCA. There is not a corresponding acknowledgement from the μ-TCA.

Table A.11: Monitoring packet.

Word	1st byte	2nd byte	Comment
1	K.28.4.	Front End number + 1 parity bit	Message in Table A.12.
2	15 bits for the message + 1 parity bit		Message in Table A.12.

A.4.3.4 Special command process (μ-TCA → Front End cards)

This process is designed to allow the μ-TCA to send special commands to the FE cards.

A register database (containing the operating mode identification) must be fixed and shared between all the detectors.

A.4.4 Data packets (Front End card → μ-TCA)

In the section the packets concerning trigger, pre-trigger and physical data are described. No acknowledgement is demanded for this kind of packets.

Pre-trigger format

Table A.12: Monitoring messages.

Item	Message	Bit[15]	...	Bit[7]	Bit[6]	Bit[5]	Bit[4]	Bit[3]	Bit[2]	Bit[1]	Comment
		Message type						Further information			
1	FPGA recon-figura-tion error	0	0	0	0	0	1	0	0	0	N/A
2	Tempe-rature alarm	0	0	0	0	1	0	x	x	x	Bit "x" is 1 if the corresponding detector goes beyond the threshold (0 elsewhere)
3	Busy	0	0	0	1	0	0	0	0	0	Front End is not able to send data
...											

Table A.13: Special command packets

Word	1st byte	2nd byte
1	K.28.3	Front End number + 1 parity bit
2	15 bits for the special command + 1 parity bit	

Table A.14: Special commands examples

Item	Command name	Bit[15..1] of 2nd word	Comment
1	System reset	"0000 0000 0001 001"	Acknowledgement packet missing
2	Counter reset	"0000 0000 0001 000"	Acknowledgement packet needed
3	Start run	"0000 0000 0000 100"	Acknowledgement packet needed
4	Stop run	"0000 0000 0000 101"	Acknowledgement packet needed
5	Dynamical FPGA configuration	"0000 0000 0000 010"	Acknowledgement packet needed
6	Veto	"0000 0000 0000 011"	Example: μ-TCA cannot receive the data. Acknowledgement packet needed

Table A.15: Control symbol for pre-trigger, trigger and physical data.

Item	Name	Control code	Comment
1	K.28.7	0xFC	The pre-trigger is generated by the THOR card and sent to the μ-TCA who shares it with the silicon layers cards.
2	K.23.7	0xF7	The trigger is generated by a single silicon layer card and sent to the μ-TCA who shares it with all the FE cards.
5	K.30.7	0xFE	The FE cards send the data.

This packet is sent to the μ-TCA by the THOR card. The μ-TCA then shares it with all the silicon FE cards.

Table A.16: Pre-trigger packet

Item	1st byte	2nd - 4th bytes
1	K.28.7	24 bits for the trigger number

Trigger format

This packet is sent back to the μ-TCA if a silicon FE card finds an interaction in coincidence after the reception of the pre-trigger packet. The trigger is always sent before the physical data packets. The μ-TCA then sends the trigger packet to all the FE cards (scatterer, absorber, hodoscope).

Table A.17: Trigger packet

Item	1st byte	2nd - 4th bytes
1	K.23.7	24 bits for the trigger number

Physical data packet format

This packet sends the "useful" data to the μ-TCA. The data format (cargo) is defined in chapter 3.

Table A.18: Physical data packet

Item	1st byte	Cargo	End of packet
1	K.30.7.	From 0 to Nbr-1 words of D characters	K.28.6 or the beginning of a new packet.

A.5 UDP packets format

Once the μ-TCA receives the data from the FE cards, a physical event is generated and stored in dedicated buffers. The buffers are then sent to the acquisition PC via UDP packets. Each detector section has its own UDP socket, and three receiving ports are used for the three data fluxes: 60001 for the hodoscope, 60002 for the absorber, 60003 for the scatterer. The content of the data buffers are sent in order to avoid to divide events in different packets, so that each UDP packet is completely independent from the others and contains complete events. The maximum size of a packet is set to 1500 (UDP data = 1472), or to 9000 for the so called "jumbo frames", used for high speed acquisitions.
Each UDP packet has a custom defined header, composed of:

- 32 bits: packet number, starting from 0;

- 16 bits: number of data structures in the packet;

The data structures are then in a list one after the other with the already described format.

A.6 Data throughput expected in clinical conditions

A.6.1 Clinical intensities

In clinical standards, the beam maximum intensity is:

- protons : 10^{10} protons/s

- carbon ions : 5×10^7 C ions/s

The Compton camera must be designed in order to be able to handle the whole range of clinical intensities. The design reference is then the maximum intensity, about 3.2 nA (2×10^{10} protons/s) delivered by the cyclotron C230 by IBA. The number of proton delivered per second is higher then the maximum considered rate (10^{10} protons/s).
As shown by the simulation results, the Compton camera can not be used for an online monitoring at the maximum beam intensity for both proton and carbon ion beams. The main limitation comes from the amount of random coincidences detected by the camera for high intensity beams. One possible solution is to deliver a lower intensity beam for the range monitoring before the beginning of the treatment. The results shown here relates to a reduced intensity, corresponding to the one selected via the simulation studies.

A.6.1.1 Review: detector and target sizes

Detectors sizes:

- Silicon scatterer : 7 silicon layers, 9.6×9.6×0.2 cm^3 (first layer 20 cm far from the beam line)

- BGO absorber: BGO block 3.5×3.8×3.0 cm^3 (67.5 cm far from the beam line - center of the block)

PMMA target size: cylindrical shape, diameter 15 cm, 20 cm length along the beam direction.

A.6.2 Coincidence rate

In the following table the coincidence and single (pre-trigger) rates expected for the different detector section are listed according to the beam kind and intensity. This values correspond the Compton camera, while for the collimated camera a reduced rate is expected for the absorber due to the presence of the physical collimator.

	Clinical intensity		Reduced intensity		Collimated camera	
	Protons	Carbon ions	Protons	Carbon ions	Protons	Carbon ions
Intensity(ions/s)	2×10^{10}	5×10^7	1×10^8	5×10^6	2×10^{10}	5×10^7
Coincidence rate per incident ion	9×10^{-4}	8×10^{-4}	9×10^{-4}	8×10^{-4}	/	/
Coincidence rate (Hz)	$1,8 \times 10^7$	4×10^4	9×10^4	4×10^3	/	/
Single rate BGO (Hz) - 96 blocks	$7,8 \times 10^7$	$1,4 \times 10^6$	$3,9 \times 10^5$	$1,4 \times 10^5$	/	/
Single rate BGO (Hz) - 1 block	$8,1 \times 10^5$	$1,5 \times 10^4$	4×10^3	$1,5 \times 10^3$	/	/
Single rate BGO (Hz) - 1 ASM card (6 blocks)	$6,5 \times 10^6$	$1,2 \times 10^5$	$3,2 \times 10^4$	$1,2 \times 10^4$	/	/

Table A.19: Coincidence and single rate as a function of the beam intensity. The BGO single rate corresponds to the pre-trigger rate.

The application of the Compton camera at clinical intensity seems not feasible. The caemra distance with respect to the beam line should be increased to lower the rate to 1×10^5 Hz (which means to put the 1

A.6.3 Data flow (Front End cards → μ-TCA)

The data format previously described has been used to evaluate the data flow between each FE card and the μ-TCA. The calculation is performed according to the "optimal" mode of each

detector. For the BGO, we only consider events where the 4 PMs are involved. For the silicon layers, two cases are considered:

- Case 1 : one single layer with 6 involved strips;

- Case 2 : all the 7 layers involved with 6 hit strips per layer.

Concerning the hodoscope, we considered an event with one hit fiber readout on the two sides.
The 8bits/10bits encoding in included in the calculation.

	Clinical intensity		Reduced intensity	
	Protons	Carbon ions	Protons	Carbon ions
Intensity (ions/s)	2×10^{10}	5×10^7	1×10^8	5×10^6
Pre-trigger flux (Mbits/s)	$2,5 \times 10^3$	47,6	13,3	4,76
Trigger flux (Mbits/s)	612	1,4	3,1	0,1
BGO data flux (Mbits/s) - 96 blocks	$1,7 \times 10^5$	373	873	37,3
BGO data flux (Mbits/s)- 1 block	$1,7 \times 10^3$	3,88	8,73	0,3
BGO data flux (Mbits/s) - 1 carte ASM	$1,4 \times 10^4$	31,1	69,9	3,1
Silicon data flux (Mbits/s) - case 1	$2,3 \times 10^5$	522	$1,2 \times 10^3$	52,2
Silicon data flux (Mbits/s) - case 2	$1,6 \times 10^6$	$3,7 \times 10^3$	$8,2 \times 10^3$	366
Hodosocpe data flux (Mbits/s)	$8,1 \times 10^4$	180	404	18

Table A.20: Data flux between FE cards and µ-TCA.

A.6.4 Acquisition data flow (µ-TCA → Acquisition PC)

The data flow from the µ-TCA to the acquisition PC is detailed here. The UDP encoding is included in the calculation.

A.6.5 Conclusions

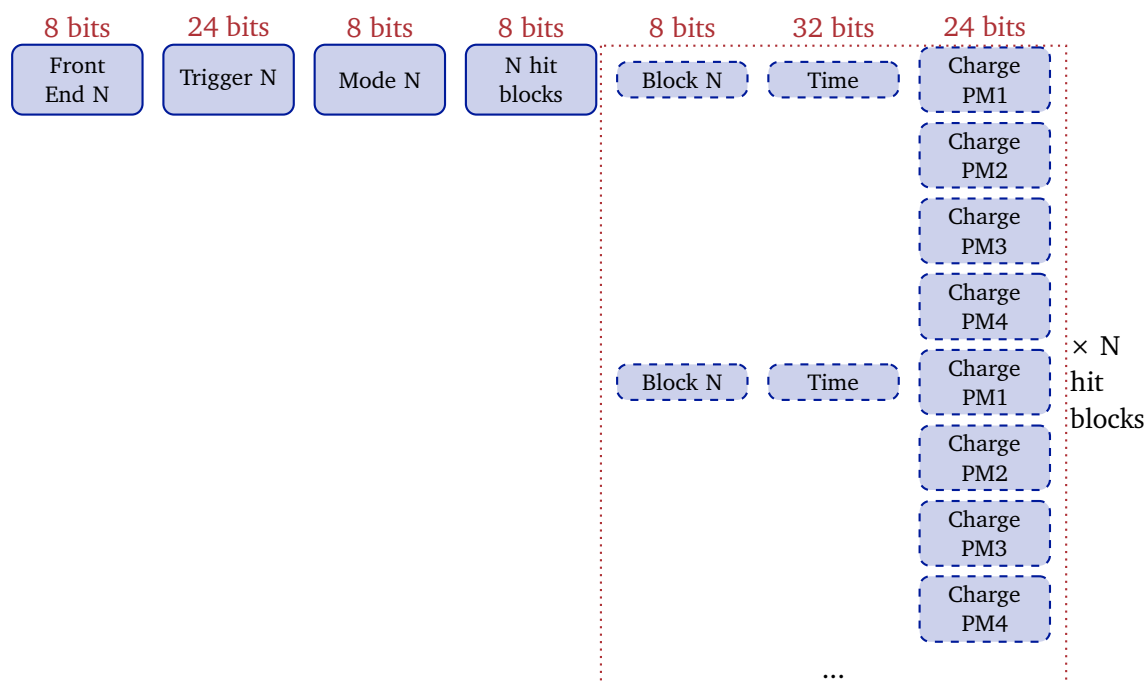As already mentioned, the Compton camera application is not feasible at clinical beam intensities.
In order to have an online monitoring of the beam range, a reduced intensity must be foreseen.
The main limitation is the rate of random coincidences detected at high intensity, while from

	Clinical intensity		Reduced intensity	
	Protons	Carbon ions	Protons	Carbon ions
Intensity (ions/s)	2×10^{10}	5×10^{7}	1×10^{8}	5×10^{6}
Coincidence rate per incident ion	9×10^{-4}	8×10^{-4}	9×10^{-4}	8×10^{-4}
Coincidence rate (Hz)	$1,8 \times 10^{7}$	4×10^{4}	9×10^{4}	4×10^{3}
Data flow (Mbits/s) - case 1	$2,2 \times 10^{4}$	46,7	112	5,0
Data flow (Mbits/s) - case 2	6×10^{4}	133	300	13,3

Table A.21: Data flow between μ-TCA and acquisition PC.

the technological point of view no limitations are highlighted by this study. In the collimated camera configuration, where no coincidences are required and the random coincidences limitation is removed, we can then expect to be able to work at real clinical intensity.
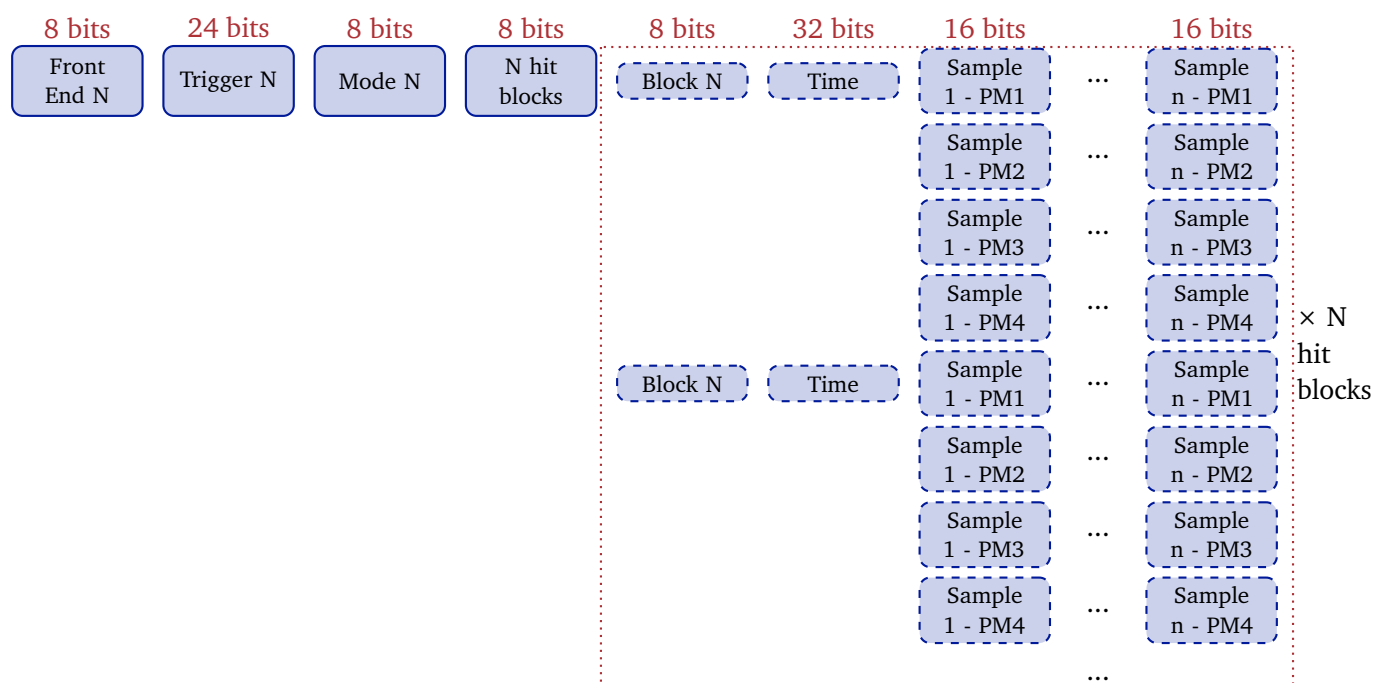
Mode 1

8 bits	24 bits	8 bits	8 bits	8 bits	32 bits	24 bits

Front End N   Trigger N   Mode N   N hit blocks

Block N   Time   Charge PM1

Charge PM2

Charge PM3

Charge PM4

Block N   Time   Charge PM1

Charge PM2

Charge PM3

Charge PM4

× N hit blocks

...

Mode 2

8 bits	24 bits	8 bits	8 bits	8 bits	32 bits	16 bits	16 bits

Front End N   Trigger N   Mode N   N hit blocks

Block N   Time   Sample 1 - PM1 ... Sample n - PM1

Sample 1 - PM2 ... Sample n - PM2

Sample 1 - PM3 ... Sample n - PM3

Sample 1 - PM4 ... Sample n - PM4

Block N   Time   Sample 1 - PM1 ... Sample n - PM1

Sample 1 - PM2 ... Sample n - PM2

Sample 1 - PM3 ... Sample n - PM3

Sample 1 - PM4 ... Sample n - PM4

× N hit blocks

...

Figure A.3: Absorber detector data format.

Mode 1

8 bits	24 bits	8 bits	8 bits	8 bits	32 bits	
Front End N	Trigger N	Mode N	N hit fibers	Fiber N	Time	× N hit fibers
				Fiber N	Time	
					...	

Mode 2

8 bits	24 bits	8 bits	16 bits	16 bits	16 bits	16 bits	8 bits	32 bits	
Front End N	Trigger N	Mode N	N fiber charge 1	Charge 1	N fiber charge 2	Charge 2	Fiber N	Time	× N hit fibers
							Fiber N	Time	
								...	
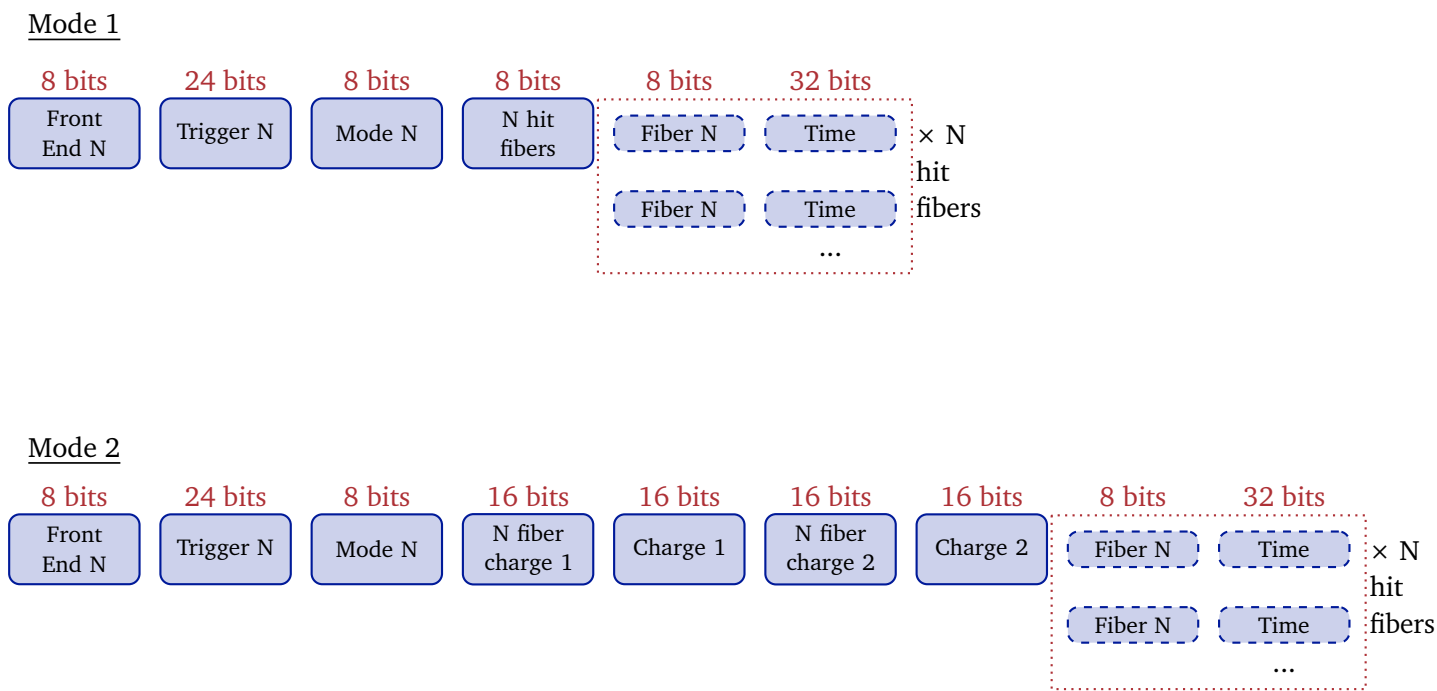
Figure A.4: Beam hodoscope data format.

Figure A.5: Architecture of communication between DAQ cards and μ-TCA.
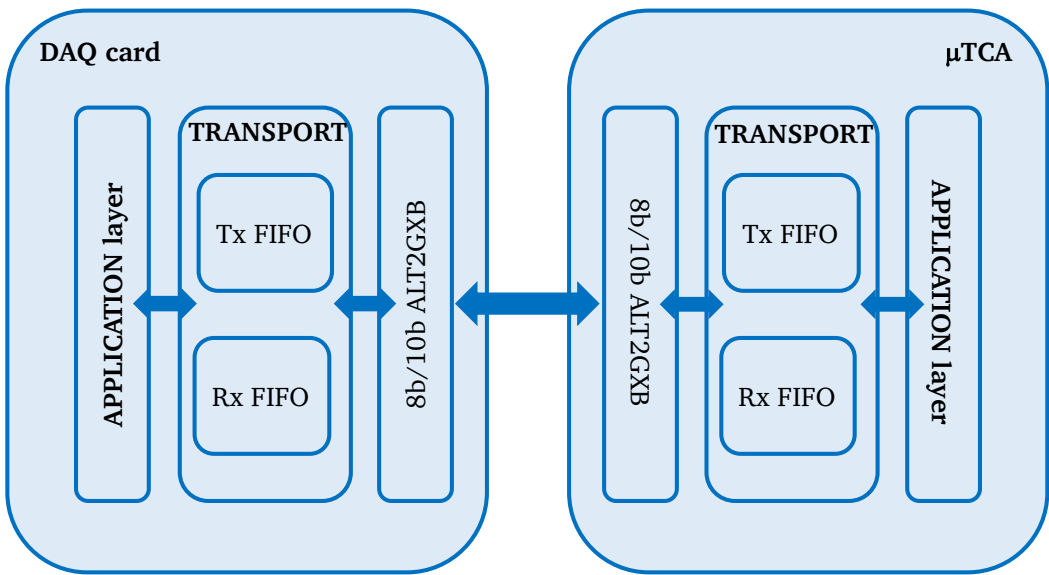
B

Electronics specifications

Acronyms

BGO Bismuth Germanium Oxide - $Bi_{12}GeO_{20}$. vii, 21, 22, 30

CdTe Cadmium Telluride. 22

CLaRyS Contrôle en Ligne de lâhadronthérapie par Rayonnements Secondaires - Online monitoring of ion beam therapy through secondary particles. 12, 18, 19, 29, 33, 35

CPPM Centre de Physique des Particules de Marseille. 12

CREATIS Centre de Recherche en Acquisition et Traitement de l'Image pour la Santé. 12, 22

ENC Equivalent Noise Charge. 21

FWHM Full Width at Half Maximum. 21, 22

GANIL Grand Accelerateur National d'Ions Lourds. 21

GATE GEANT4 Application for Tomographic Emission. 23

GEANT4 GEometry And Tracking 4. 19

HEGP High Energy General Purpose. 24

IPNL Institut de Physique Nucléaire de Lyon. 12

LM-MLEM List Mode-Maximum Likelihood Expectation Maximization. 22, 30

LPC Laboratoire de Physique de Clermont. 12

LPSC Laboratoire de Physique Subatomique et Corpuscolaire. 12

MEGAlib Medium-Energy Gamma-ray Astronomy library. 22

NaI(Tl) Sodium Iodide doped with Thallium. 23–25

PET Positron Emission Tomography. 12, 18

Acronyms

SPECT Single Photon Emission Computed Tomography. 18, 19, 23, 33

TOF Time-Of-Flight. 12

Bibliography

Anger, H. O. (1958). "Scintillation Camera". In: *Review of Scientific Instruments* 29.1, pp. 27–33. DOI: 10.1063/1.1715998. eprint: http://dx.doi.org/10.1063/1.1715998. URL: http://dx.doi.org/10.1063/1.1715998 (cit. on p. 18).

Anger, H. O. (1964). "Scintillation Camera with Multichannel Collimators". In: *Journal of Nuclear Medicine* 5.7, pp. 515–531. eprint: http://jnm.snmjournals.org/content/5/7/515.full.pdf+html. URL: http://jnm.snmjournals.org/content/5/7/515.short (cit. on p. 18).

Bhat, M. R. (1992). *Evaluated Nuclear Structure Data File (ENSDF), Nuclear Data for Science and Technology, page 817, edited by S. M. Qaim (SpringerVerlag, Berlin, Germany, 1992)*. URL: https://www.nndc.bnl.gov/ (visited on 03/27/2017) (cit. on p. 20).

Cecchin, D., D. Poggiali, L. Riccardin, P. Turco, F. Bui, and S. De Marchi (2015). "Analytical and experimental FWHM of a gamma camera: theoretical and practical issues." In: *PeerJ 3:e722* (cit. on p. 27).

Everett, D. B., J. S. Fleming, R. W. Todd, and J. M. Nightingale (1977). "Gamma-radiation imaging system based on the Compton effect". In: *Proceedings of the Institution of Electrical Engineers* 124.11, pp. 995–. ISSN: 0020-3270. DOI: 10.1049/piee.1977.0203 (cit. on p. 18).

Fontana, M., D. Dauvergne, J. M. Létang, J.-L. Ley, and É. Testa (2017a). "Compton camera study for high efficiency SPECT and benchmark with Anger system". In: *Physics in Medicine and Biology* 62.23, p. 8794. URL: http://stacks.iop.org/0031-9155/62/i=23/a=8794 (cit. on p. 17).

Fontana, M., D. Dauvergne, J.-L. Ley, J. M. Létang, V. Maxim, and É. Testa (2017b). "Versatile Compton camera for high energy gamma rays: Monte Carlo comparison with Anger camera for medical imaging". In: *2nd Jagiellonan Symposium on Fundamental and Applied Subatomic Physics*. Vol. 48. Krakow, Poland, pp. 1639–1645. DOI: 10.5506/APhysPolB.48.1639. URL: https://hal.archives-ouvertes.fr/hal-01609541 (cit. on p. 17).

GE Healthcare (June 2006). "Infinia". In: Release 2.5 (cit. on pp. 18, 23).

Han, L., W. L. Rogers, S. S. Huh, and N. Clinthorne (2008). "Statistical performance evaluation and comparison of a Compton medical imaging system and a collimated Anger camera for higher energy photon imaging". In: *Physics in Medicine and Biology* 53.24, p. 7029. URL: http://stacks.iop.org/0031-9155/53/i=24/a=002 (cit. on pp. 18, 19, 21, 33).

Hubbell, J. H. and M. J. Berger (1987). *XCOM: Photon Cross Sections on a Personal Computer, Report NBSIR 87-3597 (1987), National Institute for Standards and Technology, U.S.A.* URL: http://physics.nist.gov/PhysRefData/XrayMassCoef/ (visited on 02/21/2017) (cit. on pp. 25, 34).

Kabuki, S., K. Hattori, R. Kohara, E. Kunieda, A. Kubo, H. Kubo, K. Miuchi, T. Nakahara, T. Nagayoshi, H. Nishimura, Y. Okada, R. Orito, H. Sekiya, T. Shirahata, A. Takada, T. Tanimori,

and K. Ueno (2007). "Development of Electron Tracking Compton Camera using micro pixel gas chamber for medical imaging". In: *Nuclear Instruments and Methods in Physics Research Section A: Accelerators, Spectrometers, Detectors and Associated Equipment* 580.2. Imaging 2006, pp. 1031–1035. ISSN: 0168-9002. DOI: https://doi.org/10.1016/j.nima.2007.06.098. URL: http://www.sciencedirect.com/science/article/pii/S0168900207013186 (cit. on p. 35).

Kuchment, P. and F. Terzioglu (2016). "3D Image Reconstruction from Compton camera data". In: arXiv: 1604.03805 [physics.data-an] (cit. on p. 35).

Lojacono, X., M.-H. Richard, J.-L. Ley, É. Testa, C. Ray, N. Freud, J. M. Létang, D. Dauvergne, V. Maxim, and R. Prost (2013). "Low Statistics Reconstruction of the Compton Camera Point Spread Function in 3D Prompt-gamma Imaging of Ion Beam Therapy". In: *IEEE Transactions on Nuclear Science* 60.5, pp. 3355–3363. ISSN: 0018-9499. DOI: 10.1109/TNS.2013.2275200 (cit. on p. 22).

Nurdan, T. C., K. Nurdan, A. B. Brill, and A. H. Walenta (2015). "Design criteria for a high energy Compton Camera and possible application to targeted cancer therapy". In: *Journal of Instrumentation* 10.07, p. C07018. URL: http://stacks.iop.org/1748-0221/10/i=07/a=C07018 (cit. on p. 19).

Richard, M.-H. (2012). "Design study of a Compton camera for prompt-gamma imaging during ion beam therapy". PhD thesis. Università© Claude Bernard - Lyon I (cit. on p. 13).

Singh, M. (1983). "An electronically collimated gamma camera for single photon emission computed tomography. Part I: theoretical considerations and design criteria". In: *Medical Physics* 10.4, pp. 421–427. ISSN: 2473-4209. DOI: 10.1118/1.595313. URL: http://dx.doi.org/10.1118/1.595313 (cit. on p. 18).

Sonoda, S., Y. Ichimura, H. Kimura, S. Kabuki, A. Takada, T. Mizmoto, H. Kubo, S. Miyamoto, S. Komura, T. Takemura, T. Sawano, T. Kishimoto, Y. Matsuoka, Y. Mizumura, and T. Tanimori (2015). "Application of Electron Tracking Compton Camera (ETCC) in medical imaging". In: *2015 IEEE Nuclear Science Symposium and Medical Imaging Conference (NSS/MIC)*, pp. 1–3. DOI: 10.1109/NSSMIC.2015.7582015 (cit. on p. 35).

Zoglauer, A., R. Andritschke, and F. Schopper (2006). "MEGAlib The Medium Energy Gamma-ray Astronomy Library". In: *New Astronomy Reviews* 50, pp. 629–632. DOI: 10.1016/j.newar.2006.06.049 (cit. on p. 22).

Index

Acknoledgements